Jet structure from dihadron correlations in d + Au collisions at $\sqrt{s_{NN}} = 200$ GeV

S. S. Adler,[5] S. Afanasiev,[20] C. Aidala,[10] N. N. Ajitanand,[44] Y. Akiba,[21,40] A. Al-Jamel,[35] J. Alexander,[44] K. Aoki,[25] L. Aphecetche,[46] R. Armendariz,[35] S. H. Aronson,[5] R. Averbeck,[45] T. C. Awes,[36] V. Babintsev,[17] A. Baldisseri,[11] K. N. Barish,[6] P. D. Barnes,[28] B. Bassalleck,[34] S. Bathe,[6,31] S. Batsouli,[10] V. Baublis,[39] F. Bauer,[6] A. Bazilevsky,[5,41] S. Belikov,[17,19] M. T. Bjorndal,[10] J. G. Boissevain,[28] H. Borel,[11] M. L. Brooks,[28] D. S. Brown,[35] N. Bruner,[34] D. Bucher,[31] H. Buesching,[5,31] V. Bumazhnov,[17] G. Bunce,[5,41] J. M. Burward-Hoy,[27,28] S. Butsyk,[45] X. Camard,[46] P. Chand,[4] W. C. Chang,[2] S. Chernichenko,[17] C. Y. Chi,[10] J. Chiba,[21] M. Chiu,[10] I. J. Choi,[53] R. K. Choudhury,[4] T. Chujo,[5] V. Cianciolo,[36] Y. Cobigo,[11] B. A. Cole,[10] M. P. Comets,[37] P. Constantin,[19] M. Csanád,[13] T. Csörgö,[22] J. P. Cussonneau,[46] D. d'Enterria,[10] K. Das,[14] G. David,[5] F. Deák,[13] H. Delagrange,[46] A. Denisov,[17] A. Deshpande,[41] E. J. Desmond,[5] A. Devismes,[45] O. Dietzsch,[42] J. L. Drachenberg,[1] O. Drapier,[26] A. Drees,[45] A. Durum,[17] D. Dutta,[4] V. Dzhordzhadze,[47] Y. V. Efremenko,[36] H. En'yo,[40,41] B. Espagnon,[37] S. Esumi,[49] D. E. Fields,[34,41] C. Finck,[46] F. Fleuret,[26] S. L. Fokin,[24] B. D. Fox,[41] Z. Fraenkel,[52] J. E. Frantz,[10] A. Franz,[5,40] A. D. Frawley,[14] Y. Fukao,[25,40,41] S.-Y. Fung,[6] S. Gadrat,[29] M. Germain,[46] A. Glenn,[47] M. Gonin,[26] J. Gosset,[11] Y. Goto,[40,41] R. Granier de Cassagnac,[26] N. Grau,[19] S. V. Greene,[50] M. Grosse Perdekamp,[18,41] H.-Å. Gustafsson,[30] T. Hachiya,[16] J. S. Haggerty,[5] H. Hamagaki,[8] A. G. Hansen,[28] E. P. Hartouni,[27] M. Harvey,[5] K. Hasuko,[40] R. Hayano,[8] X. He,[15] M. Heffner,[27] T. K. Hemmick,[45] J. M. Heuser,[40] P. Hidas,[22] H. Hiejima,[18] J. C. Hill,[19] R. Hobbs,[34] W. Holzmann,[44] K. Homma,[16] B. Hong,[23] A. Hoover,[35] T. Horaguchi,[40,41,48] T. Ichihara,[40,41] V. V. Ikonnikov,[24] K. Imai,[25,40] M. Inaba,[49] M. Inuzuka,[8] D. Isenhower,[1] L. Isenhower,[1] M. Ishihara,[40] M. Issah,[44] A. Isupov,[20] B. V. Jacak,[45] J. Jia,[45] O. Jinnouchi,[40,41] B. M. Johnson,[5] S. C. Johnson,[27] K. S. Joo,[32] D. Jouan,[37] F. Kajihara,[8] S. Kametani,[8,51] N. Kamihara,[40,48] M. Kaneta,[41] J. H. Kang,[53] K. Katou,[51] T. Kawabata,[8] A. V. Kazantsev,[24] S. Kelly,[9,10] B. Khachaturov,[52] A. Khanzadeev,[39] J. Kikuchi,[51] D. J. Kim,[53] E. Kim,[43] G.-B. Kim,[26] H. J. Kim,[53] E. Kinney,[9] A. Kiss,[13] E. Kistenev,[5] A. Kiyomichi,[40] C. Klein-Boesing,[31] H. Kobayashi,[41] L. Kochenda,[39] V. Kochetkov,[17] R. Kohara,[16] B. Komkov,[39] M. Konno,[49] D. Kotchetkov,[6] A. Kozlov,[52] P. J. Kroon,[5] C. H. Kuberg,[1,*] G. J. Kunde,[28] K. Kurita,[40] M. J. Kweon,[23] Y. Kwon,[53] G. S. Kyle,[35] R. Lacey,[44] J. G. Lajoie,[19] Y. Le Bornec,[37] A. Lebedev,[19,24] S. Leckey,[45] D. M. Lee,[28] M. J. Leitch,[28] M. A. L. Leite,[42] X. H. Li,[6] H. Lim,[43] A. Litvinenko,[20] M. X. Liu,[28] C. F. Maguire,[50] Y. I. Makdisi,[5] A. Malakhov,[20] V. I. Manko,[24] Y. Mao,[38,40] G. Martinez,[46] H. Masui,[49] F. Matathias,[45] T. Matsumoto,[8,51] M. C. McCain,[1] P. L. McGaughey,[28] Y. Miake,[49] T. E. Miller,[50] A. Milov,[45] S. Mioduszewski,[5] G. C. Mishra,[15] J. T. Mitchell,[5] A. K. Mohanty,[4] D. P. Morrison,[5] J. M. Moss,[28] D. Mukhopadhyay,[52] M. Muniruzzaman,[6] S. Nagamiya,[21] J. L. Nagle,[9,10] T. Nakamura,[16] J. Newby,[47] A. S. Nyanin,[24] J. Nystrand,[30] E. O'Brien,[5] C. A. Ogilvie,[19] H. Ohnishi,[40] I. D. Ojha,[3,50] H. Okada,[25,40] K. Okada,[40,41] A. Oskarsson,[30] I. Otterlund,[30] K. Oyama,[8] K. Ozawa,[8] D. Pal,[52] A. P. T. Palounek,[28] V. Pantuev,[45] V. Papavassiliou,[35] J. Park,[43] W. J. Park,[23] S. F. Pate,[35] H. Pei,[19] V. Penev,[20] J.-C. Peng,[18] H. Pereira,[11] V. Peresedov,[20] A. Pierson,[34] C. Pinkenburg,[5] R. P. Pisani,[5] M. L. Purschke,[5] A. K. Purwar,[45] J. M. Qualls,[1] J. Rak,[19] I. Ravinovich,[52] K. F. Read,[36,47] M. Reuter,[45] K. Reygers,[31] V. Riabov,[39] Y. Riabov,[39] G. Roche,[29] A. Romana,[26,*] M. Rosati,[19] S. S. E. Rosendahl,[30] P. Rosnet,[29] V. L. Rykov,[40] S. S. Ryu,[53] N. Saito,[25,40,41] T. Sakaguchi,[8,51] S. Sakai,[49] V. Samsonov,[39] L. Sanfratello,[34] R. Santo,[31] H. D. Sato,[25,40] S. Sato,[5,49] S. Sawada,[21] Y. Schutz,[46] V. Semenov,[17] R. Seto,[6] T. K. Shea,[5] I. Shein,[17] T.-A. Shibata,[40,48] K. Shigaki,[16] M. Shimomura,[49] A. Sickles,[45] C. L. Silva,[42] D. Silvermyr,[28] K. S. Sim,[23] A. Soldatov,[17] R. A. Soltz,[27] W. E. Sondheim,[28] S. P. Sorensen,[47] I. V. Sourikova,[5] F. Staley,[11] P. W. Stankus,[36] E. Stenlund,[30] M. Stepanov,[35] A. Ster,[22] S. P. Stoll,[5] T. Sugitate,[16] J. P. Sullivan,[28] S. Takagi,[49] E. M. Takagui,[42] A. Taketani,[40,41] K. H. Tanaka,[21] Y. Tanaka,[33] K. Tanida,[40] M. J. Tannenbaum,[5] A. Taranenko,[44] P. Tarján,[12] T. L. Thomas,[34] M. Togawa,[25,40] J. Tojo,[40] H. Torii,[25,41] R. S. Towell,[1] V-N. Tram,[26] I. Tserruya,[52] Y. Tsuchimoto,[16] H. Tydesjö,[30] N. Tyurin,[17] T. J. Uam,[32] H. W. van Hecke,[28] J. Velkovska,[5] M. Velkovsky,[45] V. Veszprémi,[12] A. A. Vinogradov,[24] M. A. Volkov,[24] E. Vznuzdaev,[39] X. R. Wang,[15] Y. Watanabe,[40,41] S. N. White,[5] N. Willis,[37] F. K. Wohn,[19] C. L. Woody,[5] W. Xie,[6] A. Yanovich,[17] S. Yokkaichi,[40,41] G. R. Young,[36] I. E. Yushmanov,[24] W. A. Zajc,[10,†] C. Zhang,[10] S. Zhou,[7] J. Zimányi,[22] L. Zolin,[20] and X. Zong[19]

(PHENIX Collaboration)

[1]*Abilene Christian University, Abilene, Texas 79699, USA*

[2]*Institute of Physics, Academia Sinica, Taipei 11529, Taiwan*

[3]*Department of Physics, Banaras Hindu University, Varanasi 221005, India*

[4]*Bhabha Atomic Research Centre, Bombay 400 085, India*

[5]*Brookhaven National Laboratory, Upton, New York 11973-5000, USA*

[6]*University of California–Riverside, Riverside, California 92521, USA*

[7]*China Institute of Atomic Energy (CIAE), Beijing, People's Republic of China*

[8]*Center for Nuclear Study, Graduate School of Science, University of Tokyo, 7-3-1 Hongo, Bunkyo, Tokyo 113-0033, Japan*

[9]*University of Colorado, Boulder, Colorado 80309, USA*

[10]*Columbia University, New York, New York 10027 and Nevis Laboratories, Irvington, New York 10533, USA*

[11]*Dapnia, CEA Saclay, F-91191, Gif-sur-Yvette, France*

[12]*Debrecen University, H-4010 Debrecen, Egyetem tér 1, Hungary*

[13]*ELTE, Eötvös Loránd University, H-1117 Budapest, Pázmány P.s. 1/A, Hungary*

[14]*Florida State University, Tallahassee, Florida 32306, USA*

[15]*Georgia State University, Atlanta, Georgia 30303, USA*
[16]*Hiroshima University, Kagamiyama, Higashi-Hiroshima 739-8526, Japan*
[17]*IHEP Protvino, State Research Center of Russian Federation, Institute for High Energy Physics, Protvino, RU-142281, Russia*
[18]*University of Illinois at Urbana-Champaign, Urbana, Illinois 61801, USA*
[19]*Iowa State University, Ames, Iowa 50011, USA*
[20]*Joint Institute for Nuclear Research, RU-141980 Dubna, Moscow Region, Russia*
[21]*KEK, High Energy Accelerator Research Organization, Tsukuba, Ibaraki 305-0801, Japan*
[22]*KFKI Research Institute for Particle and Nuclear Physics of the Hungarian Academy of Sciences (MTA KFKI RMKI), H-1525 Budapest 114, P.O. Box 49, Budapest, Hungary*
[23]*Korea University, Seoul, 136-701, Korea*
[24]*Russian Research Center "Kurchatov Institute," Moscow, Russia*
[25]*Kyoto University, Kyoto 606-8502, Japan*
[26]*Laboratoire Leprince-Ringuet, Ecole Polytechnique, CNRS-IN2P3, Route de Saclay, F-91128, Palaiseau, France*
[27]*Lawrence Livermore National Laboratory, Livermore, California 94550, USA*
[28]*Los Alamos National Laboratory, Los Alamos, New Mexico 87545, USA*
[29]*LPC, Université Blaise Pascal, CNRS-IN2P3, Clermont-Fd, F-63177 Aubiere Cedex, France*
[30]*Department of Physics, Lund University, Box 118, SE-221 00 Lund, Sweden*
[31]*Institut für Kernphysik, University of Muenster, D-48149 Muenster, Germany*
[32]*Myongji University, Yongin, Kyonggido 449-728, Korea*
[33]*Nagasaki Institute of Applied Science, Nagasaki-shi, Nagasaki 851-0193, Japan*
[34]*University of New Mexico, Albuquerque, New Mexico 87131, USA*
[35]*New Mexico State University, Las Cruces, New Mexico 88003, USA*
[36]*Oak Ridge National Laboratory, Oak Ridge, Tennessee 37831, USA*
[37]*IPN-Orsay, Universite Paris Sud, CNRS-IN2P3, BP1, F-91406, Orsay, France*
[38]*Peking University, Beijing, People's Republic of China*
[39]*PNPI, Petersburg Nuclear Physics Institute, Gatchina, Leningrad region, RU-188300, Russia*
[40]*RIKEN (The Institute of Physical and Chemical Research), Wako, Saitama 351-0198, JAPAN*
[41]*RIKEN BNL Research Center, Brookhaven National Laboratory, Upton, New York 11973-5000, USA*
[42]*Universidade de São Paulo, Instituto de Física, Caixa Postal 66318, São Paulo CEP05315-970, Brazil*
[43]*System Electronics Laboratory, Seoul National University, Seoul, South Korea*
[44]*Chemistry Department, Stony Brook University, Stony Brook, SUNY, New York 11794-3400, USA*
[45]*Department of Physics and Astronomy, Stony Brook University, SUNY, Stony Brook, New York 11794, USA*
[46]*SUBATECH (Ecole des Mines de Nantes, CNRS-IN2P3, Université de Nantes) BP 20722-44307, Nantes, France*
[47]*University of Tennessee, Knoxville, Tennessee 37996, USA*
[48]*Department of Physics, Tokyo Institute of Technology, Oh-okayama, Meguro, Tokyo 152-8551, Japan*
[49]*Institute of Physics, University of Tsukuba, Tsukuba, Ibaraki 305, Japan*
[50]*Vanderbilt University, Nashville, Tennessee 37235, USA*
[51]*Waseda University, Advanced Research Institute for Science and Engineering, 17 Kikui-cho, Shinjuku-ku, Tokyo 162-0044, Japan*
[52]*Weizmann Institute, Rehovot 76100, Israel*
[53]*Yonsei University, IPAP, Seoul 120-749, Korea*
(Received 7 October 2005; published 10 May 2006)

Dihadron correlations at high transverse momentum p_T in $d+$Au collisions at $\sqrt{s_{NN}} = 200$ GeV at midrapidity are measured by the PHENIX experiment at the Relativistic Heavy Ion Collider. From these correlations, we extract several structural characteristics of jets: the root-mean-squared transverse momentum of fragmenting hadrons with respect to the jet $\sqrt{\langle j_T^2 \rangle}$, the mean sine-squared of the azimuthal angle between the jet axes $\langle \sin^2 \phi_{jj} \rangle$, and the number of particles produced within the dijet that are associated with a high-p_T particle (dN/dx_E distributions). We observe that the fragmentation characteristics of jets in $d+$Au collisions are very similar to those in $p+p$ collisions and that there is little dependence on the centrality of the $d+$Au collision. This is consistent with the nuclear medium having little influence on the fragmentation process. Furthermore, there is no statistically significant increase in the value of $\langle \sin^2 \phi_{jj} \rangle$ from $p+p$ to $d+$Au collisions. This constrains the effect of multiple scattering that partons undergo in the cold nuclear medium before and after a hard collision.

DOI: 10.1103/PhysRevC.73.054903 PACS number(s): 25.75.−q, 13.87.−a, 24.85.+p

I. INTRODUCTION

Jet production in high energy collisions is a useful tool to study the passage of scattered partons through a nuclear

*Deceased.
†PHENIX spokesperson: zajc@nevis.columbia.edu

medium. A dominant hard-scattering process is two partons scattering to produce two high-transverse momentum (high-p_T) partons which then fragment to produce a dijet. In a nuclear environment, the partons that participate in the collision can undergo multiple scattering within the nucleus, potentially changing the structure of the dijet. Such changes can provide information on the interaction of colored partons with the cold nuclear medium.

Some information on this interaction is already available at Relativistic Heavy Ion Collider (RHIC) energies via the Cronin enhancement of the p_T spectra [1]. In d + Au collisions at RHIC [2–4], the cross section for high-p_T particle production in d + Au collisions is enhanced compared to $p + p$ collisions, consistent with multiple scattering in the cold nuclear medium increasing the transverse momentum of the partons. In this paper, we report on a complementary observable to the Cronin effect: the broadening of dijet distributions. Such broadening is directly related to the additional transverse momentum delivered to the partons during multiple scattering, and hence it provides a complementary tool for comparing experiment against theory.

Interpreting both d + Au and Au + Au collisions requires solid knowledge of baseline $p + p$ collisions, especially those dijet events at midrapidity that contain two nearly back-to-back jets produced from a hard (large Q^2) parton-parton interaction. Experimentally, the jets were not exactly back to back, and the acoplanarity momentum vector $\vec{k}_T$ was measured in $p + p$ collisions at the Intersecting Storage Rings at CERN (ISR) to have a magnitude k_T on the order of 1 GeV/c [5]. This was much larger than the magnitude expected if k_T was due to an intrinsic parton transverse momentum governed by the hadron size, which would lead to $k_T \sim 300$ MeV/c. It was realized early [6] that additional gluon radiation either before or after the hard scattering will increase the value of k_T and the dijet acoplanarity.

In collisions involving nuclei at laboratory energies from 400 to 800 GeV/c, multiple scattering within the nucleus increases the parton transverse momentum. Fermilab experiments E557 [7], E609 [8], and E683 [9] all measured an increase in the dijet acoplanarity with atomic mass of the target. In E683, they measured an $A^{\frac{1}{3}}$ dependence of $\langle k_T^2 \rangle$ for both $\gamma + A$ and $\pi + A$ collisions. This dependence is expected since the number of scatterings should be proportional to the length traversed in the nucleus ($L \sim A^{\frac{1}{3}}$). For large A, the extracted $\langle k_T^2 \rangle$ values are about 50% above those for collisions with the hydrogen target, implying that the multiple-scattering effects are as important to the broadening of the dijets as are the initial state effects at that energy. In the case of $p + A$ reactions, the measured $\langle k_T^2 \rangle$ values increase more slowly than $A^{\frac{1}{3}}$ [8]. Since the $\langle k_T^2 \rangle$ values show a strong energy dependence [9], we need to establish the initial and multiple-scattering contributions to $\langle k_T^2 \rangle$ for $p + A$ reactions at RHIC energies. The $\langle k_T^2 \rangle$ values are also known to be dependent on the Q^2 of the parton-parton interaction, increasing with rising Q^2 [10,11].

No model is currently available that can reproduce all data on the Cronin effect and dijet broadening, although most include multiple scattering as the underlying mechanism. A recent review [12] considered two large classes of models: (1) soft or Glauber scattering where the multiple scattering is at either the hadronic or partonic level and (2) semihard multiple scattering where the multiple scattering is at the partonic level.

In both the soft and hard scattering models, the increase $\Delta\langle k_T^2 \rangle = \langle k_T^2 \rangle_{p+A} - \langle k_T^2 \rangle_{p+p}$ is proportional to the product of the scattering cross section and the nuclear thickness function,

$$\Delta\langle k_T^2 \rangle \propto \nu(b, \sqrt{s}) - 1 = \sigma_{\mathrm{MS}}(\sqrt{s}) T_A(b), \tag{1}$$

where $\nu(b, \sqrt{s})$ is the number of interactions, b is the impact parameter of the collision, σ_{MS} is the multiple-scattering cross section, and $T_A(b)$ is the nuclear thickness function. For the soft scattering models, σ_{MS} is defined to be $\sigma_{NN}(\sqrt{s})$, the nucleon-nucleon scattering cross section: while for the semihard models, σ_{MS} is $\sigma_{i|H}^{N}(\sqrt{s})$, the parton-nucleon semihard cross section. In the specific case of hard sphere nucleon scattering [13],

$$\nu(b, \sqrt{s}) = \sigma_{NN}(\sqrt{s}) \frac{3A}{2\pi R^2} \sqrt{1 - \frac{b^2}{R^2}}$$

where R is the nuclear radius, which gives an $A^{\frac{1}{3}}$ increase in $\Delta\langle k_T^2 \rangle$.

Both types of these models give the same trend in centrality and the same dependence on the target's atomic mass. The difference between them is in the strength of the increase with respect to $T_A(b)$ and how this changes with beam energy. We will compare the data in this paper to two specific implementations of the hard-scattering models from Qiu and Vitev [14] and Barnafoldi *et al.* [15].

An alternative view of the Cronin effect was recently proposed by Hwa and Yang [16]. These authors calculate the recombination of hard partons with soft partons released during the multiple collisions. Because this model reproduces the measured Cronin effect at RHIC without imparting successive transverse momentum kicks to the scattered partons, the authors suggest that there may be little to no increase in k_T from $p + p$ to d + Au collisions.

We also use jet-fragmentation observables to probe multiple scattering in cold nuclei, in particular, $\sqrt{\langle j_T^2 \rangle}$, the rms of the mean transverse momentum of hadrons with respect to the fragmenting parton, and the fragmentation function of the parton, $D(z, Q^2)$, where z is the fraction of the parton's momentum that a hadron carries. If the parton suffers semihard inelastic collisions within the nuclear environment, the parton will lose energy and its subsequent hadronization will produce fewer high-z fragments and more low-z fragments. We cannot directly measure fragmentation functions via dihadron correlations, but we can measure the distribution of hadrons produced in association with a high-p_T trigger particle. We plot these distributions as a function of x_E, where x_E is defined as

$$x_E = \frac{\vec{p}_{T,\mathrm{trig}} \cdot \vec{p}_{T,\mathrm{assoc}}}{|\vec{p}_{T,\mathrm{trig}}|^2}. \tag{2}$$

The motivation for the variable x_E can be most easily seen in the simple case where $\langle z \rangle = 1$ for the trigger particle and the two hadrons are emitted back to back. In this case, $p_{T,\mathrm{trig}}$ is the transverse momentum of the scattered parton

($q_{T,\mathrm{parton}}$), and for the far side, $x_E = z_{\mathrm{assoc}} = p_{T,\mathrm{assoc}}/q_{T,\mathrm{parton}}$. Relaxing the assumption on z_{trig}, there is still a simple relation between x_E and z for back-to-back jets at high p_T, where $x_E \simeq z_{\mathrm{assoc}}/z_{\mathrm{trig}}$. Hence the dN/dx_E distribution for hadrons emitted back to back from the trigger hadron can be related to the fragmentation function; for more details, see the end of Sec. II.

There is considerable information on x_E distributions from $p + p$ collisions. The CCHK Collaboration [5] demonstrated that the x_E distribution scaled, i.e., the distribution was approximately independent of $p_{T,\mathrm{trig}}$. Scaling at higher $p_{T,\mathrm{trig}}$ was also established by Fisk *et al.* [17] and the CCOR Collaboration [18,19], providing support for the idea that fragmentation of high-p_T partons is independent of the momentum of the parton.

This scaling is, however, approximate, and scaling violation was understood by Feynman *et al.* [6] to be caused by the radiation of semihard gluons. Scaling violation of the fragmentation function $D(z, Q^2)$ is now well established experimentally ([20] and references therein). For the Q^2 range considered in this paper ($10 < Q^2 < 1000\ \mathrm{GeV}/c^2$), the fragmentation functions used in next-to-leading order (NLO) calculations [21] drop by 25% for $z = 0.6$ over the range $10 < Q^2 < 100\ \mathrm{GeV}/c^2$. At higher Q^2, the fragmentation functions are less dependent on Q^2, e.g., the fragmentation drops by less than 20% at $z = 0.6$ over the much larger range of $100 < Q^2 < 1500\ \mathrm{GeV}/c^2$.

In this paper, we quantify the extent to which our measured x_E distributions in d + Au collision scale, and we compare the x_E distributions to those from $p + p$ collisions at RHIC. The goal is to establish whether inelastic scattering in the cold medium or the recombination mechanism changes the effective fragmentation function. The x_E distributions provide a stringent test of the recombination model from Hwa and Yang [22]. This model reproduces the Cronin effect in d + Au collisions through a shower thermal recombination mechanism and predicts an increase in jet-associated multiplicity [22,23], i.e., an increase in the near-angle dN/dx_E, in d + Au relative to $p + p$ collisions.

The measured x_E distributions in d + Au also serve as a critical baseline for Au + Au collisions, where the strong energy loss in the dense, hot medium is expected to dramatically change the shape of these distributions.

Our three goals for this paper are (1) to report the characteristics of jet structures in d + Au collisions at RHIC energies, (2) to establish the extent to which multiple scattering changes these structures as a function of centrality and by comparison with data from $p + p$ collisions, and (3) to establish the baseline for jet-structure measurements in heavy ion reactions. Any difference between jet properties in Au + Au and d + Au collisions should be attributable to the hot, dense nuclear matter created in the heavy ion collisions. The main results in this paper are presented in Sec. IV, which details the measured values of $\langle j_T^2 \rangle$ and $\langle \sin^2 \phi_{jj} \rangle$ and the p_T and x_E distributions from d + Au collisions at $\sqrt{s_{NN}} = 200$ GeV. These results are derived from the fitted widths and yields of two-particle azimuthal correlations, which are reported in Sec. IV. The experimental methods used to obtain these correlations are described in Sec. III, and the jet quantities we use throughout the paper are fully defined in Sec. II.

II. JET ANGULAR (AZIMUTHAL) CORRELATIONS

A. Two-particle correlation

The defining characteristic of a jet is the production of a large number of particles clustered in a cone in the direction of the fragmenting parton. Traditionally, energetic jets are identified directly using standard jet reconstruction algorithms [24,25]. In heavy ion collisions, the large amount of soft background makes direct jet reconstruction difficult. Even in $p + A$ or $p + p$ collisions, the range of energy accessible to direct jet reconstruction is probably limited to $p_T > 5{-}10\ \mathrm{GeV}/c$, below which the jet cone becomes too broad and contamination from the "underlying event" background is significant. Jet identification is even more complicated for detectors with limited acceptance, such as the PHENIX central arms, because of leakage of the jet cone outside the acceptance.

The two-particle azimuthal angle correlation technique provides an alternative way to access the properties of jets. It is based on the fact that the fragments are strongly correlated in azimuth ϕ and pseudorapidity η. Thus, the jet signal manifests itself as a narrow peak in $\Delta\phi$ and $\Delta\eta$ space. Jet properties can be extracted on a statistical basis by accumulating many events to build a $\Delta\phi$ distribution or a $\Delta\phi$ correlation function. Furthermore, we assume that the soft background is isotropic. Distributions in $\Delta\phi$ were initially used in the 1970s to search for jet signals in $p + p$ collisions at CERN's ISR facility [5,10,26]. More recently, $\Delta\phi$ distributions and correlation functions have been exploited for analysis of jet correlations at RHIC [27–31]. A detailed discussion of the two-particle correlation method can be found in [32]. These approaches overcome problems due to background and limited acceptance, and they extend the study of jet observables to lower p_T.

In the correlation method, two classes of particles are correlated with each other: trigger particles and associated particles. Although the distinction between these two classes is artificial, trigger particles are typically selected from a higher p_T range. In this work, we distinguish between two primary categories of correlations:

(i) Assorted-p_T correlation, where the p_T ranges for the trigger and associated particles do not overlap.
(ii) Fixed-p_T correlation, where the p_T ranges for the trigger and associated particles are identical.

In this paper, correlations are further categorized via a scheme which uses the identity of the trigger and associated particles. Denoting the trigger-particle p_T as $p_{T,\mathrm{trig}}$ and associated-particle p_T as $p_{T,\mathrm{assoc}}$, we present four different types of such correlations:

(i) $h^{\pm} - h^{\pm}$ fixed-p_T correlations. The p_T range of both the trigger and associated particle is $1 < p_T < 5\ \mathrm{GeV}/c$.

(ii) $h^{\pm} - h^{\pm}$ assorted-p_T correlations. There are three different selections:
   (a) $2.5 < p_{T,\mathrm{trig}} < 4\ \mathrm{GeV}/c$ with $0.5 < p_{T,\mathrm{assoc}} < 2.5\ \mathrm{GeV}/c$.
   (b) $4 < p_{T,\mathrm{trig}} < 6\ \mathrm{GeV}/c$ with $0.5 < p_{T,\mathrm{assoc}} < 4\ \mathrm{GeV}/c$.
   (c) $3 < p_{T,\mathrm{trig}} < 5\ \mathrm{GeV}/c$ with $0.5 < p_{T,\mathrm{assoc}} < 3\ \mathrm{GeV}/c$.

(iii) $\pi^0 - h^{\pm}$ assorted-p_T correlations. The trigger particle is a neutral pion and the associated particle is a charged hadron, where $5 < p_{T,\mathrm{trig}} < 10\ \mathrm{GeV}/c$ with $1 < p_{T,\mathrm{assoc}} < 5\ \mathrm{GeV}/c$.

(iv) $\pi^{\pm} - h^{\pm}$ assorted-p_T correlations. The trigger particle is a charged pion and the associated particle is a charged hadron, where $5 < p_{T,\mathrm{trig}} < 16\ \mathrm{GeV}/c$ with $1 < p_{T,\mathrm{assoc}} < 5\ \mathrm{GeV}/c$.

For each type of correlation, we study jet structure as a function of centrality and the momentum of the trigger and associated particles.

B. Extraction of j_T, $\sin^2\phi_{jj}$ from the correlation function

In this section, we discuss the framework for the two-particle correlation method. Figures 1 and 2 illustrate the relation between the two particles and their parent jet when the parents are the same jet or the dijet, respectively. The figures also show the relationship between j_T, $\sin^2(\phi_{jj})$, and the kinematic variables describing the trigger and associated particle. j_T is the component of the particle momentum perpendicular to the jet momentum. Its projection into the azimuthal plane is j_{T_y}. The quantity p_{out} (denoted with N or F for near or far side, respectively) is the component of the associated particle's p_T that is perpendicular to the trigger particle's p_T. The vector sum of $k_{T,1}$ and $k_{T,2}$ produces the dijet acoplanarity, and the azimuthal angle between the jet axes is ϕ_{jj}.

The rms value of j_{T_y} can be derived from the correlation functions. For the single jet fragmentation of Fig. 1, if we denote $\Delta\phi$, ϕ_{tj}, and ϕ_{aj} as the angles between trigger-associated, trigger-jet, and associated-jet, respectively, then the following relations are true:

$$\sin(\phi_{tj}) = \frac{j_{T_y,\mathrm{trig}}}{p_{T,\mathrm{trig}}} \equiv x_{j,\mathrm{trig}},$$
$$\sin(\phi_{aj}) = \frac{j_{T_y,\mathrm{assoc}}}{p_{T,\mathrm{assoc}}} \equiv x_{j,\mathrm{assoc}},$$

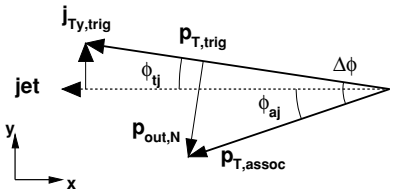

FIG. 1. Near-side or single jet fragmentation kinematics in the azimuthal plane perpendicular to the beam axis. Angles ϕ_{tj} and ϕ_{aj} are the angles (in the plane transverse to the beam axis) between the trigger-jet and associated-jet axes, respectively. Also shown are the p_T vectors for the trigger and associated particles, as well as p_{out} and j_{T_y} of the trigger particle.

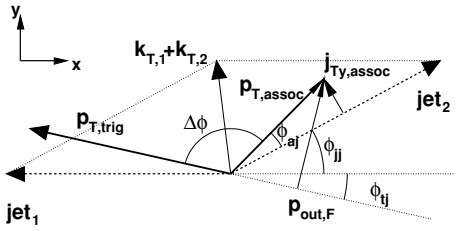

FIG. 2. Far-side jet fragmentation kinematics in the azimuthal plane perpendicular to the beam axis. Similar to Fig.1, the ϕ indices aj, jj, and tj denote the angles between the associated-jet, jet-jet, and trigger-jet axes.

$$\sin(\Delta\phi) = \frac{p_{\mathrm{out},N}}{p_{T,\mathrm{assoc}}},$$
$$\Delta\phi = \phi_{tj} + \phi_{aj}. \tag{3}$$

Assuming ϕ_{tj} and ϕ_{aj} are statistically independent, we have (cross terms average to 0) for the near side,

$$\langle \sin^2 \Delta\phi_N \rangle = \langle \sin^2 \phi_{tj} \rangle \cos^2 \phi_{aj} + \langle \sin^2 \phi_{aj} \rangle \cos^2 \phi_{tj}. \tag{4}$$

Substituting the sine and cosine terms from Eq. (3) into Eq. (4), we obtain the equation for the rms value of j_{T_y}

$$\sqrt{\left\langle j_{T_y}^2 \right\rangle} = \sqrt{\langle p_{\mathrm{out},N}^2 \rangle / \left(1 + \langle x_h^2 \rangle - 2\langle x_{j,\mathrm{trig}}^2 \rangle\right)}, \tag{5}$$

where $x_h = p_{T,\mathrm{assoc}}/p_{T,\mathrm{trig}}$.

In the Gaussian approximation for the near-side azimuthal distributions, a simple Taylor expansion connects p_{out} with the jet width σ such that

$$\left\langle p_{\mathrm{out}}^2 \right\rangle = \left\langle p_{T,\mathrm{assoc}}^2 \sin^2 \Delta\phi \right\rangle \approx \left\langle p_{T,\mathrm{assoc}}^2 \right\rangle \left[\sin\langle \Delta\phi^2 \rangle - \frac{\langle \Delta\phi^4 \rangle}{3} \right]$$
$$\approx \left\langle p_{T,\mathrm{assoc}}^2 \right\rangle [\sin\sigma^2 - \sigma^4]. \tag{6}$$

Since Eq. (5) contains the variable $x_{j,\mathrm{trig}}$ that depends on j_{T_y}, we should calculate $\sqrt{\langle j_{T_y}^2 \rangle}$ iteratively. In cases when trigger and associated particle p_T are much larger than the typical j_T value, the near-side jet width σ_N is small and $x_{j,\mathrm{trig}} \approx 0$. Hence Eq. (5) can be simplified as

$$\sqrt{\left\langle j_{T_y}^2 \right\rangle} \simeq \frac{\sigma_N \langle p_{T,\mathrm{assoc}} \rangle}{\sqrt{1 + \langle x_h^2 \rangle}} \simeq \sigma_N \frac{\langle p_{T,\mathrm{trig}} \rangle \langle p_{T,\mathrm{assoc}} \rangle}{\sqrt{\langle p_{T,\mathrm{trig}} \rangle^2 + \langle p_{T,\mathrm{assoc}} \rangle^2}}. \tag{7}$$

Since j_{T_y} is the projection of hadron p_T perpendicular to $p_{T,\mathrm{jet}}$, j_{T_y} is necessarily less than p_T. So, for any given p_T range, there is always an upper kinematic cutoff on the j_{T_y} distribution. This effect, known as the "seagull effect", leads to a reduction in the observed $\sqrt{\langle j_{T_y}^2 \rangle}$ from the expected value. It is important at low $p_{T,\mathrm{trig}}$ and becomes negligible once $p_{T,\mathrm{trig}} \gg \sqrt{\langle j_{T_y}^2 \rangle}$. The seagull effect can be parametrized and removed from the j_{T_y} values [33].

For the far-side correlation from Fig. 2 we have

$$\pi - \Delta\phi_F = \phi_{tj} + \phi_{aj} + \phi_{jj},$$
$$\sin(\Delta\phi_F) = \frac{p_{\mathrm{out},F}}{p_{T,\mathrm{assoc}}}, \tag{8}$$

where ϕ_{jj} is the azimuthal angle between the two jet axes. Expanding $\sin^2 \Delta\phi_F$ and dropping all cross terms (which average to 0), we get

$$\begin{aligned}\langle \sin^2 \Delta\phi_F \rangle = &\langle (\sin\phi_{tj} \cos\phi_{aj} \cos\phi_{jj})^2 \rangle \\ &+ \langle (\sin\phi_{aj} \cos\phi_{tj} \cos\phi_{jj})^2 \rangle \\ &+ \langle (\sin\phi_{jj} \cos\phi_{aj} \cos\phi_{tj})^2 \rangle \\ &+ \langle (\sin\phi_{tj} \sin\phi_{aj} \sin\phi_{jj})^2 \rangle. \end{aligned} \quad (9)$$

We substitute Eq. (4) to get

$$\begin{aligned}&\langle \sin^2 \Delta\phi_F \rangle \\ &= \langle \sin^2 \Delta\phi_N \rangle \langle \cos^2 \phi_{jj} \rangle + \langle \cos^2 \Delta\phi_N \rangle \langle \sin^2 \phi_{jj} \rangle \\ &= \langle \sin^2 \Delta\phi_N \rangle \langle 1 - \sin^2 \phi_{jj} \rangle + \langle 1 - \sin^2 \Delta\phi_N \rangle \langle \sin^2 \phi_{jj} \rangle \\ &= \langle \sin^2 \Delta\phi_N \rangle + \langle \sin^2 \phi_{jj} \rangle - 2 \langle \sin^2 \Delta\phi_N \rangle \langle \sin^2 \phi_{jj} \rangle. \end{aligned} \quad (10)$$

Collecting terms in ϕ_{jj} produces

$$\langle \sin^2 \phi_{jj} \rangle = \frac{\langle \sin^2 \Delta\phi_F \rangle - \langle \sin^2 \Delta\phi_N \rangle}{1 - 2\langle \sin^2 \Delta\phi_N \rangle}. \quad (11)$$

Note that since ϕ_{jj} is the azimuthal angle between the jet axes, $\sin^2(\phi_{jj})$ is one measure of the extent to which the jets are not back to back, and hence it is a quantity that is sensitive to any additional scattering in d + Au collisions. We express the right side in terms of the observables σ_N and σ_F, the rms widths of distribution that we measure by expanding the sine term

$$\langle \sin^2 \Delta\phi \rangle = \sigma^2 - \sigma^4 + 2/3\sigma^6, \quad (12)$$

which is good to 2% for rms widths at 0.5 rad and good to 0.6% for rms widths of 0.2 rad. Therefore,

$$\langle \sin^2 \phi_{jj} \rangle = \frac{\left(\sigma_F^2 - \sigma_F^4 + 2/3\sigma_F^6\right) - \left(\sigma_N^2 - \sigma_N^4 + 2/3\sigma_N^6\right)}{1 - 2\left(\sigma_N^2 - \sigma_N^4 + 2/3\sigma_N^6\right)}. \quad (13)$$

The right-hand side is now in terms of experimental observables which we will use to extract $\sin(\phi_{jj})$.

We have attempted to extract k_T from $\sin^2(\phi_{jj})$. This requires assumptions on the scattered quark distribution, the magnitude of the momentum asymmetry between the partons due to the k_T kick, as well as the detailed shape of the fragmentation function. The current paper is focused on the comparison between $p + p$ and d + Au collisions, which can be made with $\sin^2(\phi_{jj})$. Hence, we leave the extraction of k_T to future work.

In this paper, we report the rms values of j_T and $\sin(\phi_{jj})$, where $\sqrt{\langle j_T^2 \rangle} = \sqrt{2}\sqrt{\langle j_{T_y}^2 \rangle}$. In the literature, a j_T value is sometimes reported as the geometrical mean $\langle |j_{T_y}| \rangle$. The relation to the rms value is $\langle |j_{T_y}| \rangle = \sqrt{2/\pi}\sqrt{\langle j_{T_y}^2 \rangle}$.

C. Conditional yields

We also present in this paper the associated yield per trigger particle, referred to as the conditional yield (CY), as a function of p_T and x_E. CY is the number of particles produced in the same or opposite jet associated with a trigger particle,

$$\mathrm{CY}(p_T) = \frac{1}{N_{\mathrm{trig}}} \frac{dN_h}{dp_T}, \quad (14)$$

$$\mathrm{CY}(x_E) = \frac{1}{N_{\mathrm{trig}}} \frac{dN_h}{dx_E}, \quad (15)$$

and can be directly extracted from the measured Gaussian yields in the correlation functions.

To emphasize the importance of the CY, we note that it is related to the single- and two-particle cross sections:

$$\mathrm{CY} = \frac{d^2\sigma}{dp_a dp_b} \Big/ \frac{d\sigma}{dp_T}. \quad (16)$$

The interpretation for the two-particle cross section depends on whether one is studying the near- or far-side jet correlations. The conditional yield for particles from the near-side jet depends on the dihadron fragmentation function, while the conditional yield from the far side jet depends on two independent fragmentation functions: one parton fragments to produce a hadron with $p_{T,\mathrm{trig}}$, while the other scattered parton on the far side fragments to produce a hadron with $p_{T,\mathrm{assoc}}$. For the far side conditional yield at high p_T, $x_E \simeq z_{\mathrm{assoc}}/z_{\mathrm{trig}}$ [see Eq. (2)]. Hence, $d(x_E) \simeq d(z_{\mathrm{assoc}})/z_{\mathrm{trig}}$, and the slope of the far-side $\mathrm{CY}(x_E)$ is z_{trig} times the slope of the fragmentation function $D(z)$.

III. EXPERIMENT AND DATA ANALYSIS

A. Data collection

The data presented in this paper were collected by the PHENIX experiment at the RHIC facility during the d + Au and $p + p$ run of January–May 2003. During that time, integrated luminosities were recorded of 2.7 nb^{-1} for d + Au collisions and 0.35 pb^{-1} for $p + p$ collisions each at $\sqrt{s_{NN}} =$ 200 GeV.

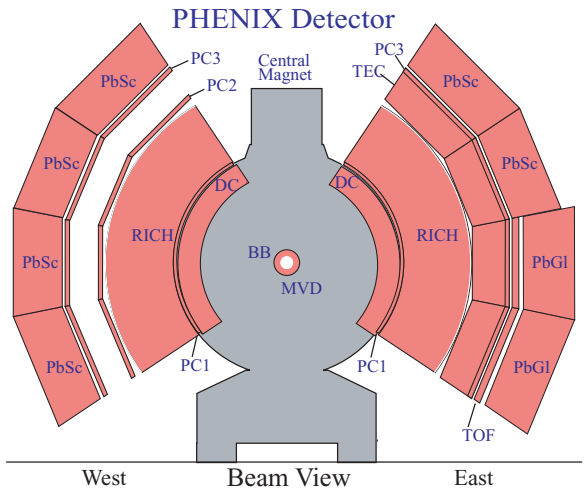

FIG. 3. (Color online) Two central spectrometer arms of the PHENIX experiment used to collect the charged hadron and charged and neutral pion tracks.

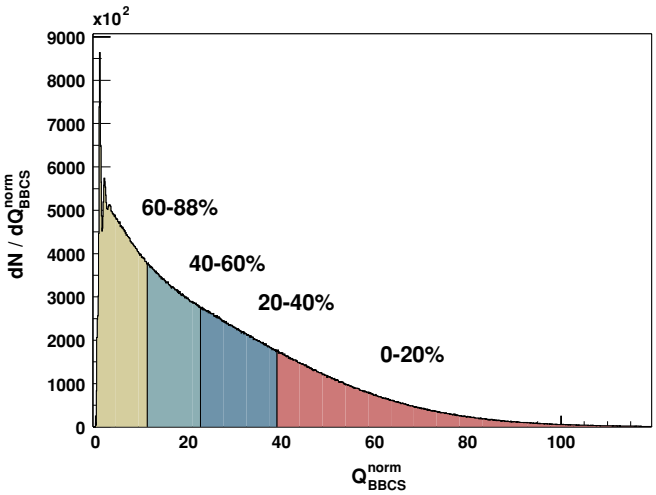

FIG. 4. (Color online) Total charge distribution on the Au-going side BBC for d + Au collisions and the centrality selection (see Table I).

The PHENIX detector consists of two central spectrometer arms, two forward muon arms, and several global detectors used for triggering, vertex detection, and centrality selection. This analysis utilizes the two central spectrometer arms that each cover a region of $|\eta| < 0.35$ units of pseudorapidity and 90° in azimuth. The spectrometer arms are not exactly back to back in azimuth; so while there is large acceptance for the detection of two particles separated by 180°, there is also finite acceptance for two particles separated by 90°. Figure 3 shows a beam cross-section view of the PHENIX central spectrometer arms. A complete overview of the whole PHENIX detector is found in Ref. [34]. In this section, we will only focus on those subsystems relevant to the analysis of the dihadron data.

1. Global event characteristics

For event characterization, the beam-beam counters (BBCs) [35] are utilized. The BBCs are sets of 64 Cherenkov counters placed symmetrically along the beam line, covering $3 < |\eta| < 3.9$ units of pseudorapidity and located 144 cm from the center of the interaction region. The BBCs determine the initial collision time t_0 and the event vertex from the time difference between particles reaching each BBC. For this analysis, we include only events with an offline cut of $|z_{\text{vertex}}| < 30$ cm.

The BBC facing the direction of the Au beam was used to determine the centrality. Figure 4 shows the BBC charge distribution and the centrality classes used in this analysis. The centrality is defined as

$$\%\text{Centrality} = 88.5\%(1 - \text{frac}(Q_{\text{BBC}})), \tag{17}$$

where $\text{frac}(Q_{\text{BBC}})$ is the fraction of the total BBC charge distribution integrated from zero to Q_{BBC}, and 88.5% is the efficiency of the minimum-bias trigger. This centrality can be related to the mean number of Au participants $\langle N_{\text{part}} \rangle$ and mean number of collisions $\langle N_{\text{coll}} \rangle$. To determine the centrality, we model the BBC charge distribution as a negative binomial distribution with a width and mean proportional to N_{part}. So, for a given centrality, several negative binomial distributions (defined by N_{part}) contribute to the overall distribution, and as such N_{part} is not uniquely defined. We calculate a weighted average of N_{part}, where the weight is given by the negative binomial distribution for a given N_{part} and the probability for having a collision with N_{part}. The latter probabilities were computed using a Glauber model, with a Hulthen wave function for the deuteron and an inelastic cross section of 42 mb. Finally, the $\langle N_{\text{coll}} \rangle$ was determined for a given $\langle N_{\text{part}} \rangle$ from the same Glauber model. The resulting centrality bins and $\langle N_{\text{coll}} \rangle$ used in this analysis are outlined in Table I.

TABLE I. Mean number of collisions for d + Au, N_{coll}, the percentage of the total inelastic cross section, and nuclear overlap function $T_A(b)$.

Percent σ_{inel}	$\langle N_{\text{coll}} \rangle$	$\langle T_A(b) \rangle (\text{mb}^{-1})$
0–20%	15.4 ± 1.0	0.367 ± 0.024
20–40%	10.6 ± 0.7	0.252 ± 0.017
40–88%	4.7 ± 0.3	0.112 ± 0.007

The dihadron events were recorded using several different level-1 triggers. The minimum-bias trigger required at least one hit in each of the BBCs and a collision vertex (computed online) that satisfies $|z_{\text{vertex}}| < 75$ cm. It was sensitive to 88.5% of the inelastic d + Au cross section. PHENIX also employed a series of level-1 triggers to select electrons, photons, and, with lower efficiency, high-p_T hadrons. These triggers utilized the ring imaging cherenkov (RICH) for electron identification, together with the electromagnetic calorimeter (EMC) [36], which consists of eight sectors, six of which are lead-scintillator (PbSc) sampling calorimeters and two are lead-glass (PbGl) Cherenkov counters. The EMC has excellent timing and energy resolution for electromagnetic showers. The triggers are called EMC/RICH triggers (ERTs) and were produced by summing signals from tiles, which were 4×5 photomultipliers (PMTs) in the RICH and either 2×2 or 4×4 PMTs in the EMC.

The electron trigger was defined by the coincidence between the minimum-bias trigger and the RICH and EMC 2×2 triggers where the threshold for the RICH tile was three photo-electrons and the EMC threshold varied between 400 and 800 MeV. Three different thresholds were available for the 4×4 photon triggers. These thresholds differed between the PbGl and PbSc and varied within and between the $p + p$ and d + Au runs. The lowest threshold setting (1.4–2.8 GeV) was most sensitive to hadron showers in the EMC. The threshold values and rejection factors (rejection = $N_{\text{minBiasEvents}}/N_{\text{triggerEvents}}$) for the ERT triggers, in coincidence with the minimum-bias trigger, are given in Table II. The $h^{\pm} - h^{\pm}$ correlations use only the minimum-bias-triggered data, while the $\pi^0 - h^{\pm}$ correlations use only the ERT photon triggers. The $\pi^{\pm} - h^{\pm}$ correlations use the minimum-bias, ERT photon, and ERT electron triggers. Above the energy threshold, the ERT electron trigger typically reached an efficiency of approximately 75%, and the ERT photon triggers reached efficiencies of 85–90%. A detailed knowledge of the ERT trigger efficiency is not necessary, since we present

TABLE II. EMC threshold and rejection factors for the electron and photon ERT triggers in coincidence with the minimum-bias trigger for $p + p$ and $d +$ Au. The photon triggers are defined by the energy sum of 4×4 PMTs in the EMC above threshold. The electron trigger requires the coincidence of the RICH trigger (threshold of three photoelectrons for both $p + p$ and $d +$ Au runs) and the energy sum of 2×2 PMTs in the EMC above threshold.

	$p + p$		$d +$ Au		$p + p$	$d +$ Au
	PbSc threshold (GeV)	PbGl threshold (GeV)	PbSc threshold (GeV)	PbGl threshold (GeV)	Rejection	Rejection
Gamma 1	2.1	2.1	2.8	3.5	400–1200	125–300
Gamma 2	2.8	2.8	2.8–3.5	3.5–4.2	1500–3100	450–900
Gamma 3	1.4	1.4	2.1	2.8	70–160	15–60
Electron	0.4–0.8	0.4–0.8	0.6–0.8	0.6–0.8	5–1200	30–170

the conditional yield distributions per trigger, for which this efficiency cancels out.

2. Tracking and particle identification

In this section, we discuss the tracking and identification of the particles used in the different correlation analyses. Three types of particles are included. Charged hadrons are used in all analyses, neutral pions are used as trigger particles for the $\pi^0 - h^\pm$ correlations, and charged pions are used as trigger particles for the $\pi^\pm - h^\pm$ correlations.

Charged hadron tracks are measured outside the PHENIX central magnetic field by the drift chamber (DC), located 2.0 m from the vertex, and two layers of multiwire proportional chamber (PC1 and PC3), located 2.5 and 5.0 m, respectively, from the vertex [37]. The DC determines the momentum and the azimuthal position of the track, while PC1 determines the polar angle [38]. The momentum resolution is determined to be $0.7\% \oplus 1.1\% p$ (GeV/c) [2]. Tracks are confirmed by requiring that an associated hit in PC3 lies within a 2.5σ (for $h^\pm - h^\pm$) or 3σ (for $\pi - h^\pm$) matching window in both the ϕ and z directions. This cut reduces the background from particles not originating in the direction of the vertex. The remaining background tracks are mainly decays and conversion particles [39]. The background level for single tracks is less than 5% below 3 GeV/c, increasing to about 30% at 5 GeV/c. However, the background is smaller for high-p_T triggered events (see Sec. III B). The charged particle tracking efficiency for the active region of the DC, PC1, and PC3 is better than 98%. Since we perform a pair analysis, the two-track resolution is important. For the DC, the two-track separation is better than 1.5 mm, while at PC1 it is 4 cm, and at PC3 it is 8 cm.

Neutral pions are detected by the statistical reconstruction of their $\gamma\gamma$ decay channel. These decay photons are detected by the EMC and identified by their time of flight (TOF) and shower shape. The electromagnetic shower shape is typically characterized by the χ^2 variable [36],

$$\chi^2 = \sum_i \frac{\left(E_i^{\text{meas}} - E_i^{\text{pred}}\right)^2}{\sigma_i^2}, \tag{18}$$

where E_i^{meas} is the energy measured at tower i and E_i^{pred} is the predicted energy for an electromagnetic particle of total energy $\sum_i E_i^{\text{meas}}$. This χ^2 value is useful for the discrimination of electromagnetic from hadron showers. The χ^2 and TOF cuts used give a very clean sample of photons with contamination of other particles at $\ll 1\%$.

Using pairs of photons that pass these EMC cuts, we create the invariant mass spectra for each photon pair p_T. A sample invariant mass distribution with a signal/background S/B of approximately 12 is given in Fig. 5. The background distribution can be reproduced by mixing clusters from different events and normalizing that distribution to the real event distribution outside the π^0 mass region. The peak position and width of the invariant mass distribution were parametrized as a function of pair p_T, in order to select π^0 candidates from a region of invariant mass within 2σ of the peak position. The S/B for a π^0 with $p_T > 5$ GeV is 10−20, increasing as a function of p_T. There is a slight dependence on centrality with the $\pi^0 S/B$ decreasing with increasing centrality.

PHENIX identifies high momentum charged pions with the RICH and EMC detectors. Charged particles with velocities above the Cherenkov threshold of $\gamma_{\text{th}} = 35$ (CO_2 radiator) emit Cherenkov photons, which are detected by photomultiplier tubes (PMTs) in the RICH [40]. This threshold corresponds to 18 MeV/c for electrons, 3.5 GeV/c for muons, and 4.9 GeV/c for charged pions. In a previous PHENIX publication [39], we showed that charged particles with reconstructed p_T above

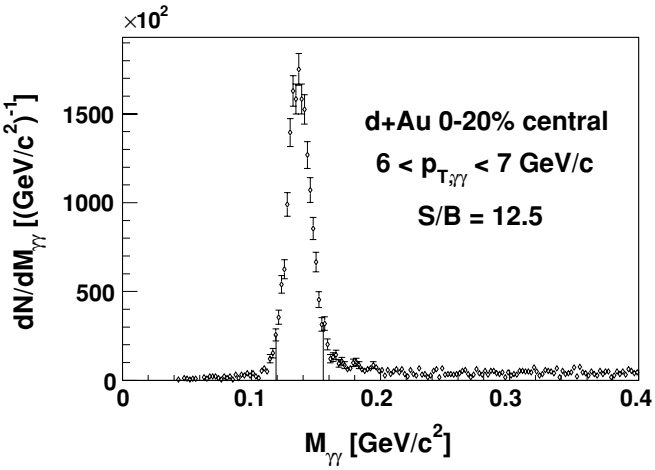

FIG. 5. Measured $\gamma\gamma$ invariant mass distribution for $6 < p_T < 7$ GeV/c in central $d +$ Au collisions. The peak is fitted with a Gaussian to extract the centroid mass and σ. The S/B within 2σ of the centroid ranges from ∼6 at 3 GeV/c up to 20 at ∼8 GeV/c.

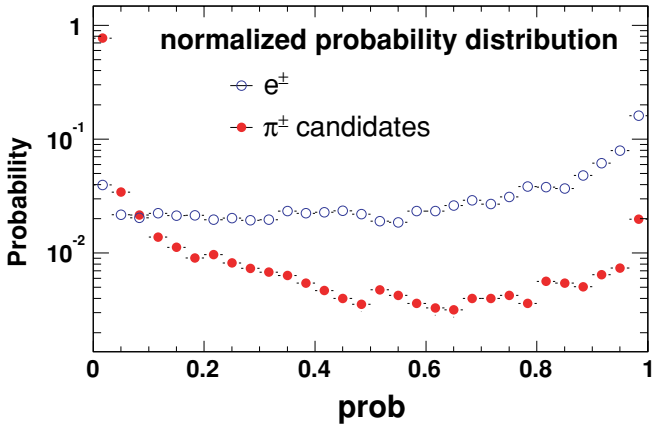

FIG. 6. (Color online) Probability distribution for charged pion candidates and electrons. Histogram integral has been normalized to unity.

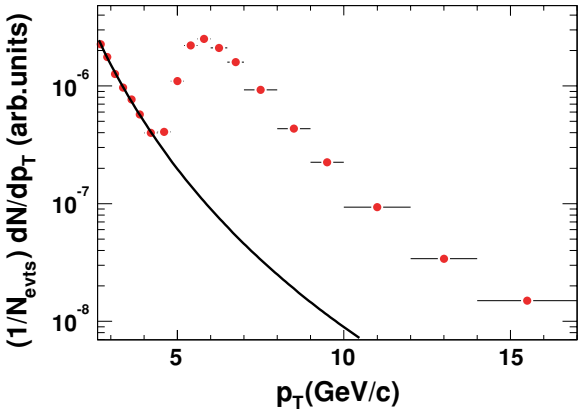

FIG. 7. (Color online) Raw charged pion transverse momentum spectrum, with the final cuts applied. Remaining background level is estimated from an extrapolation from low p_T and is shown as a black line.

4.9 GeV/c, which have an associated hit in the RICH, are dominantly charged pions and background electrons from photon conversions. The efficiency for detecting charged pions rises quickly past 4.9 GeV/c, reaching an efficiency of >90% at $p_T > 6$ GeV/c.

To reject the conversion backgrounds in the pion candidates, the shower information at the EMC is used. Since most of the background electrons are genuine low-p_T particles that were misreconstructed as high-p_T particles, simply requiring a large deposit of shower energy in the EMC is very effective in suppressing the electron background. In this analysis, a momentum-dependent energy cut applied at EMC is

$$E > 0.3 + 0.15\, p_T. \tag{19}$$

In addition to this energy cut, the shower shape information [36] is used to further separate the broad hadronic showers from the narrow electromagnetic (EM) showers and hence reduce the conversion backgrounds. In this analysis, we use the probability (prob) calculated from the χ^2 value [Eq. (18)] for an EM shower. The probability values range from 0 to 1, with a flat distribution expected for an EM shower and a peak around 0 for a hadronic shower. Figure 6 shows the probability distribution for the pion candidates and electrons, normalized by the integral, where the pion candidates were required to pass the energy cut and the electrons were selected using particle ID cuts similar to that used in Ref. [41]. Indeed, the electron distribution is relatively flat, while the charged pions peak at 0. A cut of prob <0.2 selects pions above the energy cut with an efficiency of $\gtrsim$80%. Detailed knowledge of the pion efficiency is not necessary, since we present in this paper the per-trigger pion conditional yield distributions, for which this efficiency cancels out.

Since the energy and prob cuts are independent of each other, we can fix one cut and then vary the second to check the remaining background level for conversions. The energy cut in Eq. (19) is chosen such that the raw pion yield is found to be insensitive to the variation in prob. Figure 7 shows the raw pion spectra for ERT-triggered events as a function of p_T, with the above cuts applied. The pion turnon from 4.9 to 7 GeV/c is clearly visible. Below a p_T of 5 GeV/c, the remaining background comes mainly from the random association of charged particles with hits in the RICH detector. The background level is less than 5% from 5 to 16 GeV/c, which is the p_T range for the charged pion data presented in this paper.

B. Data analysis

In this section, we outline the method used to obtain correlation functions and distributions. From these, we extract the jet shapes and yields outlined in Sec. II. For the extraction of the jet yield from the azimuthal distributions, we discuss how we obtain the absolute normalization of the distribution; while for the jet shape properties, j_{T_y} and $\langle \sin^2\phi_{jj} \rangle$, the absolute normalization is not necessary.

1. Correlation functions

Azimuthal correlation functions are generally defined as

$$C(\Delta\phi) \propto \frac{N_{\rm cor}(\Delta\phi)}{N_{\rm mix}(\Delta\phi)}. \tag{20}$$

Similarly, one can also define the correlation function in pseudorapidity as

$$C(\Delta\eta) \propto \frac{N_{\rm cor}(\Delta\eta)}{N_{\rm mix}(\Delta\eta)}. \tag{21}$$

The same-event pair distribution, $N_{\rm cor}(\Delta\phi)$ or $N_{\rm cor}(\Delta\eta)$, is constructed for trigger-associated particle pairs. The mixed-event pair distribution, $N_{\rm mix}(\Delta\phi)$ or $N_{\rm mix}(\Delta\eta)$, is determined by combining trigger particles with associated particles from randomly selected events.

This definition of the correlation function relies on the fact that detector acceptance and efficiency cancel out. It is therefore important that the pair efficiencies of the average mixed-event background and the average foreground distributions are the same. For this reason, we generate mixed-event distributions only for events with similar centralities and event vertices. More precisely, mixed events were required to match within ±10% centrality, and the event vertices were required to

be within ±3 cm. For $h^{\pm} - h^{\pm}$ correlations, the real and mixed events are minimum-bias data. For $\pi^0 - h^{\pm}$ correlations, the real and mixed events are ERT-triggered data. For $\pi^{\pm} - h^{\pm}$ correlations, the real events are ERT-triggered and minimum-bias data, while the mixed events mix ERT-triggered events with minimum-bias events.

For $h^{\pm} - h^{\pm}$ and $\pi^{\pm} - h^{\pm}$ correlations, due to finite two-track resolution for charged particles at the DC and PC, the reconstruction efficiency for same-event charged track pair drops at small $\Delta\phi$ and $\Delta\eta$. To minimize the difference in the pair efficiency between $N_{\rm cor}(\Delta\phi)$ and $N_{\rm mix}(\Delta\phi)$, the pairs are required to have a minimal separation of about two times the resolution at the various tracking detectors. This corresponds to about 0.28, 8, and 15 cm at the DC, PC1, and PC3, respectively. However, these pair cuts are not required for $\pi^0 - h^{\pm}$ correlations, because different detector subsystems are used for reconstructing trigger-π^0 and the associated charged tracks as outlined earlier.

Given the similarity of the analysis techniques between $\Delta\phi$ and $\Delta\eta$ correlations, in this paper we focus on the $\Delta\phi$ correlation. The $\Delta\phi$ correlation functions are obtained with two different normalizations. For $h^{\pm} - h^{\pm}$ assorted correlations, the correlation function is area normalized

$$C_{\rm norm}(\Delta\phi) = \frac{N_{\rm cor}(\Delta\phi)}{N_{\rm mix}(\Delta\phi)} \times \frac{\int d\Delta\phi (N_{\rm mix}(\Delta\phi))}{\int d\Delta\phi (N_{\rm cor}(\Delta\phi))}. \quad (22)$$

The details concerning this normalization are discussed in Sec. IV A. The second normalization is used in both the $\pi^0 - h^{\pm}$ and $\pi^{\pm} - h^{\pm}$ correlations. It was shown in Ref. [32] that the CY can be derived from the measured correlation function with an appropriate normalization,

$$\frac{1}{N^0_{\rm trig}} \frac{dN_0}{d\Delta\phi} = \frac{R_{\Delta\eta}}{N_{\rm trig}\epsilon} \frac{\frac{dN_{\rm cor}}{d\Delta\phi}(\Delta\phi)}{\frac{2\pi N_{\rm mix}(\Delta\phi)}{\int d\Delta\phi N_{\rm mix}(\Delta\phi)}}, \quad (23)$$

where $N^0_{\rm trig}$ and $N_{\rm trig}$ are the true and detected number of triggers, respectively, and ϵ is the average single-particle efficiency for the associated particles in 2π in azimuth and ± 0.35 in pseudorapidity. $R_{\Delta\eta}$ corrects for the loss of jet pairs outside a given $\Delta\eta$ acceptance, determined by PHENIX's finite acceptance in η. This second normalization is defined so that the integral of the resulting correlation function should be $N_0/N^0_{\rm trig}$, the total number of pairs per trigger particle in a given azimuthal and η range.

For the normalization in Eq. (23), two separate efficiencies must be determined, the $\Delta\eta$ correction and the single-particle efficiency. The near-side correlation has a well-behaved peak around $\Delta\eta = 0$. As we show in Sec. IV A, the near-side jet width in $\Delta\phi$ and $\Delta\eta$ are consistent with each other within errors. So we correct the near-side yield to the full-jet yield assuming the shape of the jet is Gaussian and the widths are equal in $\Delta\phi$ and $\Delta\eta$. This correction, according to Ref. [32], is

$$R_{\Delta\eta} = \frac{1}{\int_{-0.7}^{0.7} d\Delta\eta \frac{1}{\sqrt{2\pi}\sigma} \exp\left[-\frac{\Delta\eta^2}{2\sigma^2}\right] {\rm acc}(\Delta\eta)}, \quad (24)$$

where acc($\Delta\eta$) represents the PHENIX pair acceptance function in $|\Delta\eta|$. It can be obtained by convoluting two flat distributions in $|\eta| < 0.35$, so acc($\Delta\eta$) has a simple triangular shape: acc($\Delta\eta$) = $(0.7 - |\Delta\eta|)/0.7$. The PHENIX single-particle acceptance is flat in η to within 5%.

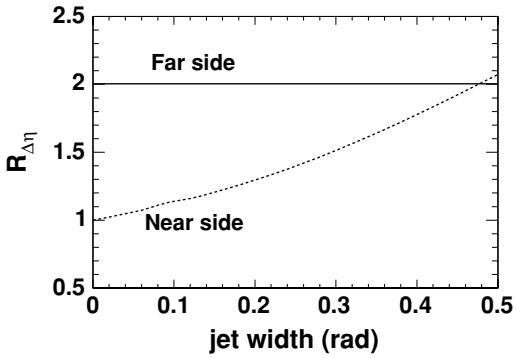

FIG. 8. Correction factor $R_{\Delta\eta}$ plotted as function of jet width for near and far sides.

In the far side, the jet signal is much broader than the PHENIX acceptance due to the broad range of momentum fraction x of the partons that participate in the hard scattering. In fact, we studied the far-side jet shape for the $\pi^{\pm} - h^{\pm}$ correlation (Fig. 17b) and found the true jet correlation strength to be almost constant in the PHENIX pair acceptance $|\Delta\eta| < 0.7$. Based on that, we assume that the far-side jet strength is constant and correct the far-side yield to the corresponding accessible pair range of $|\Delta\eta| < 0.7$,

$$R^{\rm far}_{\Delta\eta} = \frac{2 \times 0.7}{\int_{-0.7}^{0.7} d\Delta\eta \left[\frac{0.7 - |\Delta\eta|}{0.7}\right]} = 2. \quad (25)$$

$R^{\rm far}_{\Delta\eta}$ equals 2 because the pair efficiency has a triangular shape in $|\Delta\eta| < 0.7$, which results in 50% average efficiency when the real jet pair distribution is flat in $|\Delta\eta| < 0.7$. Figure 8 shows the correction factor $R_{\Delta\eta}$ as a function of jet width. The typical range of the near-side jet width in all analyses (see Sec. IV A) is below 0.5 rad. The maximum correction is about a factor of 2 for the near-side jet.

The single-particle efficiency for associated particles ϵ includes detector acceptance and reconstruction efficiency. It is evaluated in a way similar to previously published Au + Au [39] and d + Au [2] analyses. However, the jet-associated charged hadron spectrum in d + Au is much flatter than the inclusive charged hadron spectra [48],[1] so the corrections due to momentum scale and momentum resolution are much smaller than those for inclusive charged hadrons. For the same reason, the background contamination at high p_T, mainly coming from decay and photon conversions which are falsely reconstructed as high-p_T tracks [2,39], is also reduced. We studied both effects using a full GEANT simulation of PYTHIA events through PHENIX detectors. The jet-associated yields were extracted in the same manner as for the real data analysis. By comparing it with the input jet-associated yield spectra, we can quantitatively study the effect of momentum smearing and high-p_T background contamination. The corrections due to

[1]For example, in Fig. 21, the jet associated yields decrease by a factor of 100 from 0.5 to 5 GeV/c. However, the typical single inclusive hadron spectra decrease by a factor of 100 000 [2].

momentum scale and resolution are found to be less than 5% with 3% systematic errors. For high-p_T triggered events, the background contamination to the associated charged hadrons is found to be 5% independent of p_T from 1−5 GeV/c.

2. Extracting jet properties

The normalized correlation functions and conditional yield distributions are both fitted with a sum of two Gaussians to extract the jet widths and the conditional yield of hadrons in the near side ($\Delta\phi \sim 0$) and far side ($\Delta\phi \sim \pi$). The fit for the normalized correlation functions is described in Sec. IV A. For the conditional yield, we fit with the function

$$\frac{1}{N^0_{\rm trig}}\frac{dN_0}{d\Delta\phi} = B + \frac{{\rm Yield}_N}{\sqrt{2\pi}\sigma_N}\exp\left[\frac{-\Delta\phi^2}{2\sigma_N^2}\right] + \frac{{\rm Yield}_F}{\sqrt{2\pi}\sigma_F}\exp\left[\frac{-(\Delta\phi-\pi)^2}{2\sigma_F^2}\right], \quad (26)$$

where B reflects the combinatoric background level in the real distribution relative to the mixed distribution, and the other two terms represent the near-side jet and far-side jet signal, respectively. The resulting widths, σ_N and σ_F, are then used to calculate the jet shapes via Eqs. (7) and (13). For each choice of trigger and associated particle p_T range, Yield$_N$ and Yield$_F$ directly reflect the jet-associated yield $dN/dp_{T,\rm assoc}$ at the near and far side, respectively.

Two methods were used to calculate the dN/dx_E distribution. The first method was used for $\pi^0 - h^\pm$ correlations. Since these correlations are binned in p_T there is a distribution of x_E for each trigger-associated p_T bin. This distribution is approximately Gaussian. The fitted peak value is used as the bin center of the dN/dx_E distributions and the fitted Gaussian width is used as the horizontal error bar. To estimate the bin width in x_E, we used the definition Eq. (2) which can be written as (ignoring the sign) $x_E = p_{T,\rm assoc}\cos(\Delta\phi)/p_{T,\rm trig}$. We estimate $\cos(\Delta\phi) \approx 1$ and write the bin width as

$$\Delta x_E = \frac{p^{\rm max}_{T,\rm assoc} - p^{\rm min}_{T,\rm assoc}}{\langle p_{T,\rm trig}\rangle}, \quad (27)$$

where we have an associated p_T bin from $[p^{\rm min}_{T,\rm assoc}, p^{\rm max}_{T,\rm assoc}]$ and a trigger p_T bin with a mean $\langle p_{T,\rm trig}\rangle$.

The second method is adopted by $\pi^\pm - h^\pm$ analysis. It is statistically based and can be used to calculate the distribution for any pair variable $p_{T,\rm trig}$, $p_{T,\rm assoc}$, $\Delta\phi$, $\Delta\eta$, x_E, $p_{\rm out}$ etc. In the following we show two examples: the $dN/d\Delta\phi$ and dN/dx_E distributions. For each pair we calculate the $\Delta\phi$ and x_E value, then from Eq. (23) we calculate the same correction factor that was used for the $dN/d\Delta\phi$ distribution.

$$w(\Delta\phi) = \frac{R_{\Delta\eta}}{N_{\rm trig}\epsilon}\frac{1}{\frac{2\pi N_{\rm mix}(\Delta\phi)}{\int d\Delta\phi N_{\rm mix}(\Delta\phi)}}. \quad (28)$$

If this weight is used to fill the $\Delta\phi$ histogram for the real and mixed distribution, we obtain the CY for the true real pairs, and for the mixed pair the sum is,

$$\begin{aligned}{\rm background}(\Delta\phi) &= \sum_{\rm mix}\delta(\Delta\phi)w(\Delta\phi)\\ &= N_{\rm mix}(\Delta\phi)w(\Delta\phi)\\ &= \frac{N_{\rm trig}\epsilon}{R_{\Delta\eta}}\frac{\int d\Delta\phi N_{\rm mix}(\Delta\phi)}{2\pi}\end{aligned} \quad (29)$$

we have used the fact that $N_{\rm mix}(\Delta\phi) = \sum_{\rm mix}\delta(\Delta\phi)$.

Thus the jet signal can be extracted from Eq. (26) as

$$\begin{aligned}\frac{1}{N^0_{\rm trig}}\frac{dN^{\rm jet}_0}{d\Delta\phi} &= \sum_{\rm real}\delta(\Delta\phi)w(\Delta\phi) - B\\ &= \sum_{\rm real}\delta(\Delta\phi)w(\Delta\phi) - C\sum_{\rm mix}\delta(\Delta\phi)w(\Delta\phi),\end{aligned} \quad (30)$$

where

$$C = \frac{BR_{\Delta\eta}}{N_{\rm trig}\epsilon}\frac{2\pi}{\int d\Delta\phi N_{\rm mix}(\Delta\phi)}. \quad (31)$$

When this weight is used to fill the x_E histogram for both real and mixed distributions, we obtain the dN/dx_E by subtracting the mixed x_E distribution from the real x_E distribution,

$$\frac{1}{N^0_{\rm trig}}\frac{dN^{\rm jet}_0}{dx_E} = \sum_{\rm real}\delta(x_E)w(\Delta\phi) - C\sum_{\rm mix}\delta(x_E)w(\Delta\phi). \quad (32)$$

Equation (31) is rather trivial, because the weighting procedure is equivalent to Eq. (23), for which we know the shape of the distribution (Eq. (26)). But the advantage of the weighting procedure is that it allows for the determination of the absolute background pair distribution in any pair variables.

Similarly, the statistical method is used to extract the $p_{T,\rm assoc}$ and $p_{\rm out}$ spectra as

$$\frac{1}{N^0_{\rm trig}}\frac{dN^{\rm jet}_0}{dp_{T,\rm assoc}} = \sum_{\rm real}\delta(p_{T,\rm assoc})w(\Delta\phi) - C\sum_{\rm mix}\delta(p_{T,\rm assoc})w(\Delta\phi) \quad (33)$$

$$\frac{1}{N^0_{\rm trig}}\frac{dN^{\rm jet}_0}{dp_{\rm out}} = \sum_{\rm real}\delta(p_{\rm out})w(\Delta\phi) - C\sum_{\rm mix}\delta(p_{\rm out})w(\Delta\phi). \quad (34)$$

By construction, the integral of the jet yield should be conserved independent of the pair variable used, i.e.:

$$\begin{aligned}\int d\Delta\phi\frac{dN_0}{d\Delta\phi} &= \int dx_E\frac{dN^{\rm jet}_0}{dx_E}\\ \int dp_{T,\rm assoc}\frac{dN^{\rm jet}_0}{dp_{T,\rm assoc}} &= \int dp_{\rm out}\frac{dN^{\rm jet}_0}{dp_{\rm out}}.\end{aligned} \quad (35)$$

C. Systematic uncertainties

The correlation analyses presented here consist of several steps ranging from the generation of correlation functions to the extraction of the final physics variables [j_T, $\sin(\phi_{jj})$, per-trigger yields, etc.] from these correlation functions. Systematic error estimations for each of these steps have been evaluated and combined to determine the overall error quoted for each measurement. All errors quoted are maximum extent.

Systematic errors associated with the generation of correlation functions can result from shape distortions in either the foreground or background distributions. These distortions can arise if the requisite quality cuts (see Sec. III A) are not stable. In order to minimize such errors, the track pair and quality cuts were assigned such that the correlation functions were essentially insensitive to reasonable cut variations. Systematic errors associated with such cut variations are estimated to be less than 4%. A further source of systematic error is related to the efficiency of the background rejection when requiring a confirmation hit in the outer pad chamber. The yields have been corrected for remaining background. The systematic error on the background estimate is ≈3% for tracks with a transverse momentum (p_T) < 4 GeV/c and ≈7% for particles with 4 < p_T < 6 GeV/c. For the calculation of the conditional yields, the systematic error is dominated by the uncertainties associated with the determination of the efficiency corrected single-particle yields. These systematic errors have been estimated to be ≈10% as obtained from Ref. [2]. This error on the efficiency has two parts: the normalization error includes the error on PC3 matching and active area; the momentum smearing error includes contributions from momentum resolution and momentum scale.

A separate error is estimated for $\pi^0 - h^{\pm}$ correlations due to the background contamination of the π^0 within the mass bin. To estimate the width and yield contribution of the background $\gamma\gamma$ pairs, we created correlations of $\gamma\gamma$ outside the π^0 mass with hadrons. From these, we extrapolated the background contribution at the π^0 mass. These systematic errors are p_T dependent. For the near and far angle width, the variation is 1−3%, the near yield variation is 1%, the far yield variation is 1−5% and increases with increasing p_T.

The event-mixing technique has been used to correct for the limited detector acceptance and inefficiency. In addition, the CY has been corrected for limited $\Delta\eta$ coverage. To cross-check these procedures, we ran a detailed simulation using the PYTHIA event generator [42] coupled to a single-particle acceptance filter that randomly accepts charged particles according to the detector efficiency. In the following, we shall use $\pi^{\pm} - h^{\pm}$ as an example for this cross-check. Figure 9 shows a typical PHENIX two-dimensional single-particle acceptance used in this analysis.

We generated 1 million PYTHIA events, each required to have at least one >6 GeV/c charged pion. To speed up the event generation, a Q^2 cut of 100 GeV^2 on the underlying parton-parton scattering was required. These events were filtered through the single-particle acceptance filter. As an approximation, we ignore the p_T dependence of acceptance. The same event and mixed pair $\Delta\phi$ distributions were then built by combining the accepted $\pi^{\pm}$ and charged hadrons. The jet width and raw yield were extracted by fitting the $\frac{dN_{\rm fg}}{d\Delta\phi} / \frac{dN_{\rm mix}}{d\Delta\phi}$ with a constant plus double Gaussian function. The raw yields were then corrected via Eq. (24) to full jet yield for the near side and the yield in $|\Delta\eta| < 0.7$ for the far side. We also extracted the true CY and jet width without the acceptance requirement. The comparison of the CY and jet width with and without the acceptance requirement are shown in Fig. 10. The trigger particles are $\pi^{\pm}$ with 6 < $p_{T,\rm trig}$ < 10 GeV/c, the associated particles are $h^{\pm}$. In the near side, the corrected yield (top left panel) and width (bottom left panel) are compared with those extracted without the acceptance filter. In the far side, the yield corrected back to $|\Delta\eta| < 0.7$ and the width are compared with those extracted without the acceptance filter. The data requiring the acceptance filter are always indicated

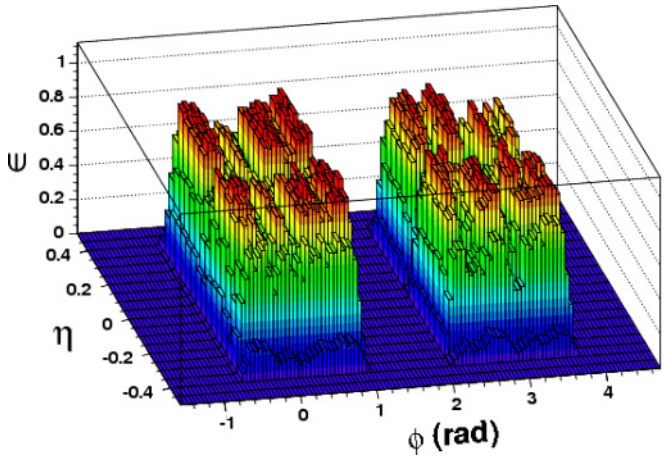

FIG. 9. (Color online) Typical PHENIX single-particle acceptance for charged hadrons.

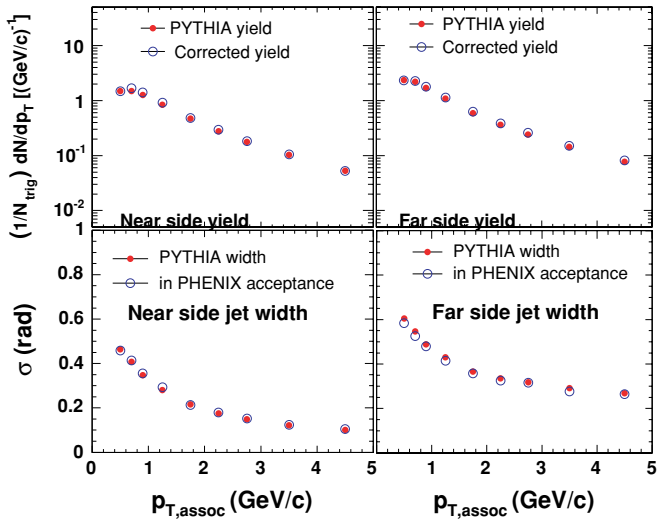

FIG. 10. (Color online) Comparison of near-side yield, near-side width, far-side yield, and far-side width as functions of p_T of charged hadrons. These are obtained for $\pi^{\pm} - h^{\pm}$ correlation from PYTHIA, with a trigger pion of 6−10 GeV/c. Filled circles represent quantities calculated with PHENIX acceptance filter.

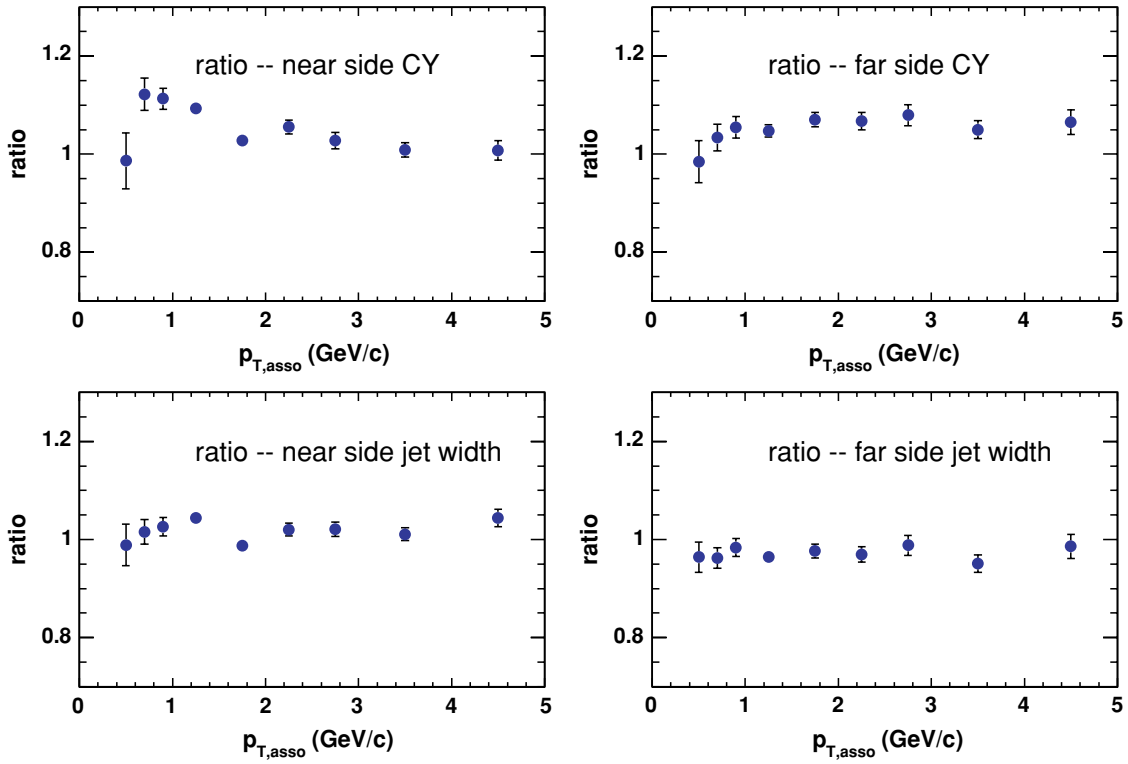

FIG. 11. (Color online) Ratio of the jet width or corrected yield obtained from the event-mixing method to those without the acceptance filter.

by the filled circles, while the expected yield or width are indicated with open circles.

The agreement between the two data sets can be better seen by plotting the ratios, which are shown in Fig. 11. The yields agree within 10% and the widths agree within 5%. Since $\sqrt{\langle j_T^2 \rangle}$, $\langle \sin^2(\phi_{jj}) \rangle$ are derived from the jet widths, the agreement in width naturally leads to the agreement in the $\sqrt{\langle j_T^2 \rangle}$ and $\langle \sin^2(\phi_{jj}) \rangle$. One notices that there are some systematic differences in the comparison of the yield at low $p_{T,\text{assoc}}$. This might indicate that the Gaussian assumption is not good enough when the jet width is wide and the extrapolation for $|\Delta\eta| > 0.7$ becomes sizable. (At $p_{T,\text{assoc}} = 0.5$ GeV/c, the jet width $\sigma_N = 0.5$ rad and the extrapolation is about 20%.)

The approximations in the formulas used to extract j_{T_y} and $\sin^2(\phi_{jj})$ are used to estimate the systematic error on these quantities. We estimate the systematic uncertainty in the formulation at the level of 5% for $\sqrt{\langle j_T^2 \rangle}$ and 3–4% for $\sqrt{\langle \sin^2(\phi_{jj}) \rangle}$.

Table III summarizes the systematic errors for the extracted widths $\sqrt{\langle j_T^2 \rangle}$ and $\sqrt{\langle \sin^2(\phi_{jj}) \rangle}$, while Tables IV, V, and VI summarize the list of systematic errors on the CY for the hadron-hadron, neutral pion-hadron, and charged pion-hadron correlations, respectively. Table VII outlines the systematic errors on the p_{out} extraction from pion-hadron correlations.

IV. RESULTS

We present the minimum-bias and centrality-dependent results on extracted jet widths and yields in Sec. IV A,

TABLE III. Summary of the systematic errors on the widths and j_T, $\langle \sin^2(\phi_{jj}) \rangle$.

Error source	
Tracking cuts, pair cuts	<4%
Assumptions used in formula	<5%
S/B correction (π^0 only)	1−3%

TABLE IV. Summary of the systematic errors on the conditional yields for $h^{\pm} - h^{\pm}$ analysis.

Error source	<4 GeV/c	4−6 GeV/c
Quality cuts	<4%	<4%
Background correction	3%	30%
Error on single particle yields	10%	10%

TABLE V. Summary of the systematic errors on the conditional yields for $\pi^0 - h^{\pm}$ analysis.

Single particle	Pair cuts		3%	
ϵ_{single}	Normalization		6.5%	
	p smearing (reso+scale)		3%	
	Near-side yield		1%	
S/B	$p_{T,\text{assoc}}$ (GeV/c)	<2	2−3	>3
	Far-side yield	5%	2%	1%

TABLE VI. Summary of the systematic errors on the conditional yields for $\pi^{\pm} - h^{\pm}$ analysis.

Single particle	Normalization			6.5%		
	p smearing (reso+scale)			3%		
ϵ_{single}	Trigger pion background			5%		
	Centrality dependent part			5%		
	$p_{T,\text{assoc}}$ (GeV/c)	<1	1−2	2−3	3−4	4−5
Yield extraction	Pair cuts	1%	1%	2%	3%	4%
	Near-side yield	20%	10%	6%	6%	6%
	Far-side yield			6%		
	Error on the fit	10−20%	6%	4%	4%	4%

TABLE VII. Summary of the systematic errors on the p_{out} distribution for $\pi^{\pm} - h^{\pm}$ analysis.

p_{out} (GeV/c)	<0.5	0.5−1	1−2	2−2.5
Yield extraction (near)	8%	15%	20%	20%
Yield extraction (far)	8%	15%	20%	30%
Other errors	10.6%	10.6%	10.6%	10.6%

which are used in Sec. IV B to calculate quantities describing the jet structures: the values of $\sqrt{\langle j_T^2 \rangle}$, $\langle \sin^2(\phi_{jj}) \rangle$, and jet fragmentation conditional yields dN/dp_T and dN/dx_E. The minimum-bias $d + \text{Au}$ results are compared with results from $p + p$ in Sec. IV C to establish the extent of effects due to medium modification in $d + \text{Au}$ with as much statistical precision as possible. The $d + \text{Au}$ centrality dependence of the derived quantities is presented in Sec. IV D. This provides a larger lever arm in nuclear thickness function, at the cost of dividing the available minimum-bias data into different centrality bins.

A. Correlation functions, widths, and yields

The baseline data from which jet structures are extracted are the correlation functions and conditional pair distributions that were defined in Sec. II. Figure 12 shows representative correlation functions between two charged hadrons, while Figs. 13 and 14 show representative conditional yield distributions triggered on neutral pions (π^0) and charged pions, respectively. All three correlation sets (Figs. 12–14) show relatively narrow peaks centered at $\Delta\phi = 0$ and π radians. The widths of these structures decrease with larger p_T, which is consistent with narrowing of the jet cone for increasing p_T. The fractional area under the jet peak relative to the flat underlying background also increases significantly as a function of associated-particle p_T, indicating increasing (di)jet

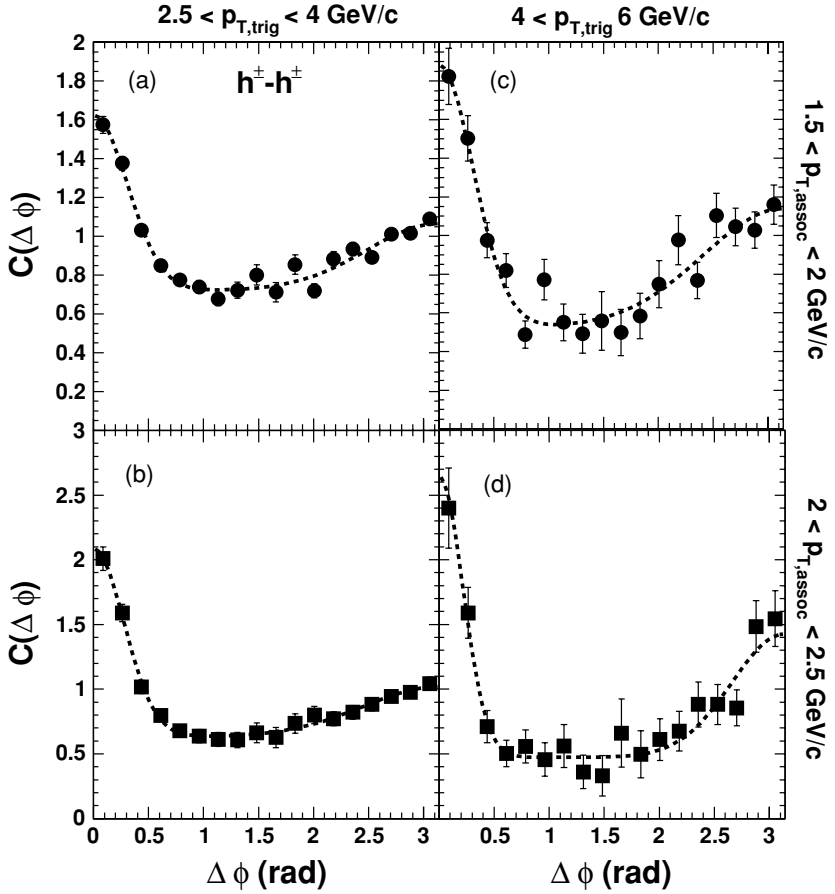

FIG. 12. Assorted $h^{\pm} - h^{\pm}$ correlation functions from $d + \text{Au}$ collisions for centrality 0–80% and several p_T cuts. Trigger p_T range is $2.5 < p_{T,\text{trig}} < 4.0$ GeV/c in (a) and (b) and $4.0 < p_{T,\text{trig}} < 6.0$ in (c) and (d). Associated hadron is in the range $1.5 < p_T < 2.0$ GeV/c or $2.0 < p_T < 2.5$ GeV/c. Correlations are for the centrality class 0−80%. Dashed line represents a fit to the correlation function using Eq. (37).

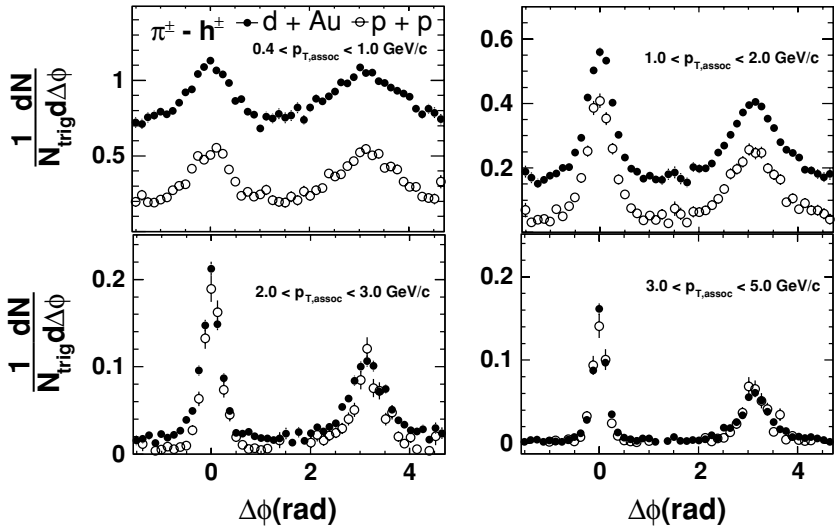

FIG. 13. Fully corrected assorted charged pion-hadron conditional pair distributions for $d+$Au collisions for centrality 0−88% and $p+p$ collisions. Trigger $\pi^{\pm}$ are within $5 < p_{T,\mathrm{trig}} < 10$ GeV/c and are correlated with hadrons with four $p_{T,\mathrm{assoc}}$ ranges as given in each plot.

contributions to the correlation function. In particular, Fig. 13 shows that for events where there is a high-p_T trigger, a large fraction of the low-p_T (as low as 0.4−1 GeV/c) particles are coming from the dijet fragmentation, and the jet contribution dominates at $p_T > 2$ GeV/c. Events tagged with a high-p_T jet are much harder than a typical minimum-bias event.

We characterize the jet correlations shown in Figs. 12–14 by assuming that there are only two contributions to the correlation function—(di)jet correlations and an isotropic underlying event. This scenario can then be expressed as

$$C(\Delta\phi) = A_o(1 + J(\Delta\phi)), \tag{36}$$

where A_o denotes the isotropic background and $J(\Delta\phi)$ is the jet function. Approximating the jet function as the sum of two Gaussians, we fit the correlations with

$$C(\Delta\phi) = A_o\left[1 + \frac{\lambda_N}{\sqrt{2\pi}\sigma_N}\exp\left(\frac{-\Delta\phi^2}{2\sigma_N^2}\right) + \frac{\lambda_F}{\sqrt{2\pi}\sigma_F} \times \exp\left(\frac{-(\Delta\phi-\pi)^2}{2\sigma_F^2}\right)\right]. \tag{37}$$

Here, $\lambda_{N,F}$ are the normalized Gaussian areas and $\sigma_{N,F}$ are the Gaussian widths for the near- and far-side jets, respectively. For the pair distribution functions, we fit with the same shaped function, but with a different normalization [Eq. (26)] as outlined in Sec. III B.

Figure 15 shows the associated-p_T dependence of the extracted widths for both the near- and far-side peaks[2] from the charged-hadron correlation functions with the trigger range for the charged hadron being 3−5 GeV/c. The data are tabulated in Table VIII.

In Fig. 16, we present the same quantities from the high-p_T identified pion correlations, where there is excellent agreement between the π^0 and charged-pion data sets. For both types of identified pions, the trigger p_T range is 5−10 GeV/c; these data are tabulated in Tables IX and X.

The far-side widths shown in Figs. 15 and 16 are larger than the near-side widths, as expected, since the far-side structure is a convolution of two jet fragmentations as well as any k_T of

[2]The results here are not sensitive to the slightly different range in centrality used.

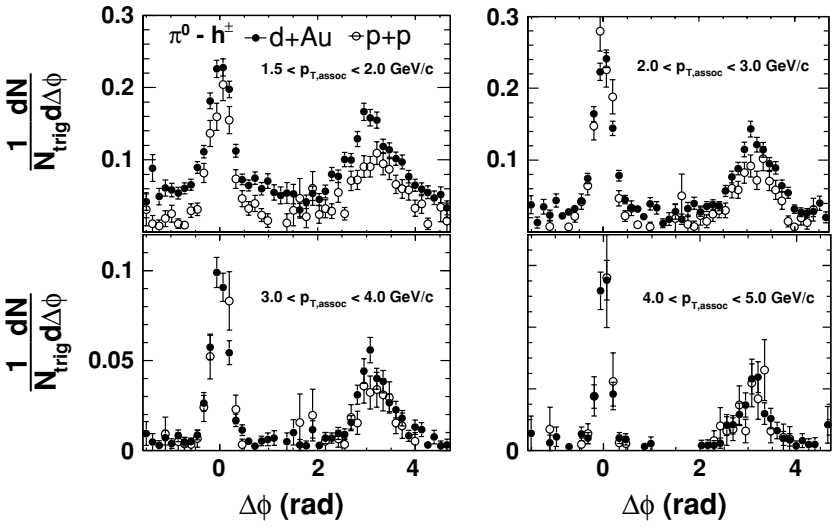

FIG. 14. Fully corrected assorted π^0-hadron conditional pair distributions for $d+$Au collisions for centrality 0−88% and $p+p$ collisions. Trigger π^0 are within $5 < p_{T,\mathrm{trig}} < 10$ GeV/c and are correlated with hadrons with four $p_{T,\mathrm{assoc}}$ ranges as given in each plot.

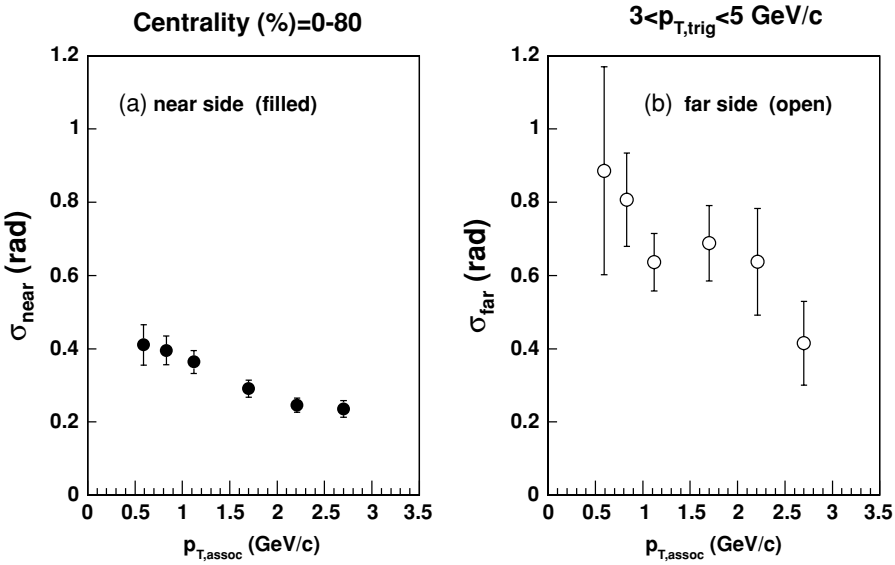

FIG. 15. Near- and far-side widths as a function of $p_{T,\mathrm{assoc}}$ for charged hadron azimuthal correlations from minimum-bias d + Au collisions (see text). Bars are statistical errors.

the scattered partons. The widths of the correlation functions also steadily decrease as a function of $p_{T,\mathrm{assoc}}$ as expected from (di)jet fragmentation. For completeness, we also tabulate the near- and far-side widths extracted as a function of $p_{T,\mathrm{trig}}$ for identified pions. These data are tabulated in Tables XI and XII.

Although the PHENIX single-particle acceptance is limited to $|\eta| < 0.35$, it can sample jet pairs in twice as large of a window in $\Delta\eta$ ($|\Delta\eta| < 0.7$) with varying pair efficiency. Similar to azimuthal correlation, the pair efficiency in $\Delta\eta$ can be estimated via mixed events and can subsequently be divided out [Eq. (21)]. Assuming that the underlying event is flat[3] in $|\Delta\eta| < 0.7$, we fix the background level to be equal to that in azimuthal correlation function Eq. (36) and subsequently extract the jet distribution as a function of $\Delta\eta$. In Fig. 17(a), we compare the near-side jet shape in $\Delta\phi$ and $\Delta\eta$ in the angular range of $|\Delta\phi, \Delta\eta| < 0.7$ for the $\pi^{\pm} - h^{\pm}$ correlation with $1.0 < p_{T,\mathrm{assoc}} < 2.0$ GeV/c. There is no significant difference

TABLE VIII. Near- and far-side widths as a function of $p_{T,\mathrm{assoc}}$ for charged hadron triggers (3−5 GeV/c) and associated charged hadrons from d + Au collisions.

$\langle p_{T,\mathrm{assoc}} \rangle$ (GeV/c)	σ_{near} (rad)	σ_{far} (rad)
0.59	0.411 ± 0.055	0.89 ± 0.28
0.83	0.395 ± 0.039	0.807 ± 0.128
1.12	0.364 ± 0.032	0.636 ± 0.079
1.7	0.291 ± 0.023	0.688 ± 0.103
2.2	0.246 ± 0.019	0.637 ± 0.146
2.7	0.236 ± 0.023	0.415 ± 0.114

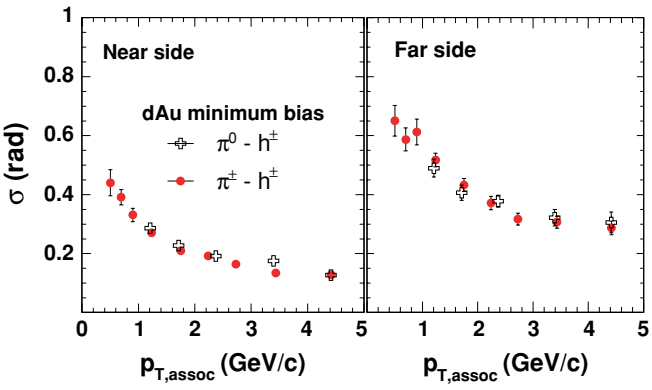

FIG. 16. (Color online) Near- and far-side widths as a function of $p_{T,\mathrm{assoc}}$ from pion-hadron azimuthal correlations for charged pion (closed symbols) and neutral pion (open symbols) triggers from the $p_{T,\mathrm{trig}}$ range of 5−10 GeV/c in minimum-bias d + Au collisions (see text). Bars are statistical errors.

[3] η dependence of the single-particle yield is very weak in $0 < |\eta| < 1$ [43]. Thus, the underlying pair distribution in $|\Delta\eta| < 0.7$ is almost flat.

TABLE IX. Near- and far-side widths as a function of $p_{T,\mathrm{assoc}}$ for charged pion triggers (5−10 GeV/c) and associated charged hadrons from minimum-bias d + Au collisions.

$\langle p_{T,\mathrm{assoc}} \rangle$ (GeV/c)	σ_{near} (rad)	σ_{far} (rad)
0.50	0.440 ± 0.044	0.651 ± 0.052
0.70	0.391 ± 0.026	0.587 ± 0.039
0.90	0.331 ± 0.023	0.613 ± 0.044
1.23	0.271 ± 0.010	0.517 ± 0.024
1.75	0.210 ± 0.008	0.433 ± 0.022
2.24	0.193 ± 0.009	0.372 ± 0.023
2.73	0.165 ± 0.007	0.317 ± 0.020
3.44	0.135 ± 0.006	0.307 ± 0.020
4.42	0.128 ± 0.008	0.287 ± 0.023

TABLE X. Same as Table IX, but for neutral pion triggers.

$\langle p_{T,\mathrm{assoc}} \rangle$ (GeV/c)	σ_{near} (rad)	σ_{far} (rad)
1.21	0.284 ± 0.011	0.494 ± 0.022
1.71	0.227 ± 0.007	0.410 ± 0.019
2.37	0.193 ± 0.005	0.380 ± 0.015
3.39	0.177 ± 0.006	0.322 ± 0.020
4.41	0.130 ± 0.007	0.315 ± 0.026

TABLE XI. Near- and far-side widths as a function of $p_{T,\mathrm{trig}}$ for charged pion triggers and associated charged hadrons (2–4.5 Gev/c) from minimum-bias d + Au collisions.

$\langle p_{T,\mathrm{trig}}\rangle$ (GeV/c)	σ_{near} (rad)	σ_{far} (rad)
5.44	0.176 ± 0.008	0.393 ± 0.030
6.31	0.165 ± 0.007	0.342 ± 0.020
7.27	0.162 ± 0.007	0.322 ± 0.022
8.60	0.157 ± 0.008	0.301 ± 0.019
10.6	0.149 ± 0.020	0.231 ± 0.039
13.2	0.177 ± 0.019	0.329 ± 0.042

in jet shape between $\Delta\eta$ and $\Delta\phi$, and the widths are consistent in both directions. Figure 17(b) shows the far-side jet shape in $\Delta\eta$; the associated pair distribution is flat within $\pm 10\%$.

Figure 18(a) shows the comparison of the near-side jet widths in $\Delta\phi$ and $\Delta\eta$ from d + Au. There is overall very good agreement between the two data sets. However, the width in $\Delta\eta$ is systematically lower than that in $\Delta\phi$ at small $p_{T,\mathrm{assoc}}$. This is because the underlying background is not completely flat in $\Delta\eta$, but varies by up to 10% in $|\Delta\eta| < 0.7$. Thus the procedure of dividing by the mixed-event distribution [Eq. (21)] introduces some distortion of the jet shape at large $\Delta\eta$ and consequently leads to a slightly different value for the jet width. In fact, for $p + p$ collisions, Fig. 18(b) indicates a similar discrepancy between $\Delta\phi$ and $\Delta\eta$ at small $p_{T,\mathrm{assoc}}$ for $p + p$ collisions. Thus this deviation is not likely due to the cold medium effect in d + Au.

We extract not only the widths of the jet structures but also the conditional yields of how many hadrons are in the near- and far-side structures for each high-p_T trigger. The conditional yield defined in Eq. (14) can be obtained from either a correlation function or conditional pair distribution, both of which produce identical results. For the conditional pair distributions, the conditional yield is directly extracted from the fit parameters [Eq. (26)]; for correlation functions, several normalization factors need to be applied to obtain the per-trigger yield [44, 45], as described below.

For correlation functions, it is convenient to define the fraction of jet-correlated particle pairs per event, $n_{\mathrm{jet\,pair}}/n_{\mathrm{total\,pair}}$. Following the basic ansatz outlined in Eq. (36), the fraction of jet-correlated particle pairs is obtained by summing the jet function over all bins in $\Delta\phi$ and dividing by the total sum of the correlation function such that

$$\frac{n_{\mathrm{jet\,pair}}}{n_{\mathrm{total\,pair}}} = \frac{\sum A_o J(\Delta\phi)}{\sum C(\Delta\phi)}. \tag{38}$$

Such pair fractions are shown as a function of $p_{T,\mathrm{assoc}}$ for a trigger hadron of $3.0 < p_T < 5.0$ GeV/c and a centrality selection of 0−80% in Fig. 19. The results, shown for both

TABLE XII. Same as Table XI, but for neutral pion triggers.

$\langle p_{T,\mathrm{trig}}\rangle$ (GeV/c)	σ_{near} (rad)	σ_{far} (rad)
5.39	0.207 ± 0.007	0.409 ± 0.025
6.40	0.151 ± 0.008	0.304 ± 0.034
7.66	0.144 ± 0.012	0.295 ± 0.035

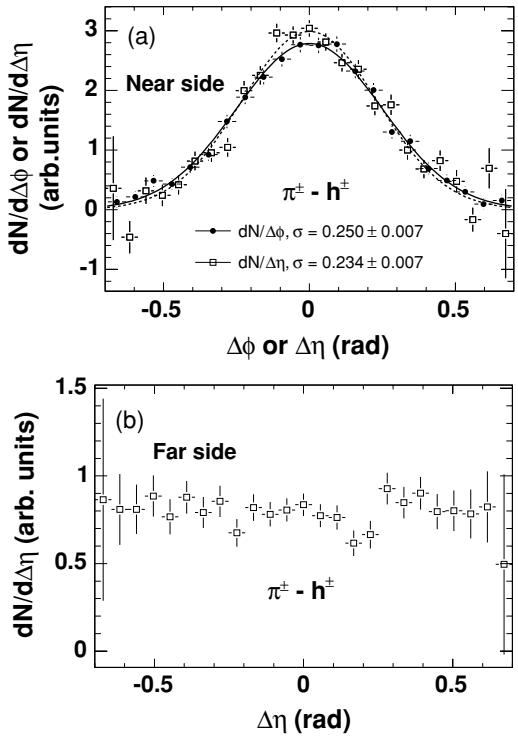

FIG. 17. Jet shapes in $\Delta\phi$ and $\Delta\eta$ from $\pi^{\pm} - h^{\pm}$ correlation with $5 < p_{T,\mathrm{trig}} < 10$ GeV/c and $1.0 < p_{T,\mathrm{assoc}} < 2.0$ GeV/c from minimum-bias d + Au collisions. (a) Near-side jet shape in $\Delta\phi$ and $\Delta\eta$. (b) Far-side jet shape in $\Delta\eta$.

the near- and far-side jets, indicate an increase in the average fraction of jet-correlated particle pairs with p_T as might be expected if jet fragmentation becomes the dominant particle production mechanism as p_T is increased.

The pair fraction is multiplied by the ratio $n_{\mathrm{pairs}}/n_{\mathrm{trig}}n_{\mathrm{assoc}}$ to obtain

$$\frac{n_{\mathrm{jet\,pair}}}{n_{\mathrm{trig}}n_{\mathrm{assoc}}} = \frac{n_{\mathrm{jet\,pair}}}{n_{\mathrm{total\,pair}}} \times \frac{n_{\mathrm{pairs}}}{n_{\mathrm{trig}}n_{\mathrm{assoc}}}, \tag{39}$$

where n_{pairs} denotes the average number of detected particle pairs per event, and n_{trig} and n_{assoc} are the detected

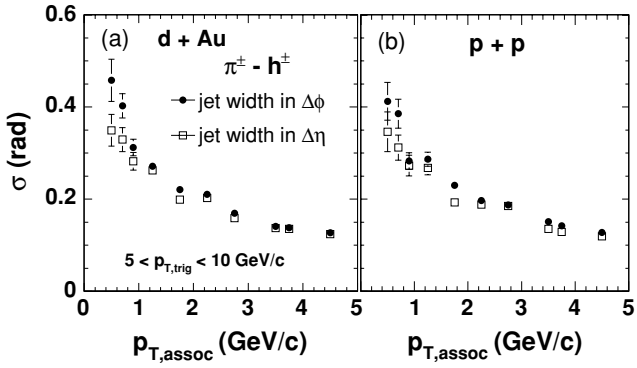

FIG. 18. Comparison of jet widths as function of $p_{T,\mathrm{assoc}}$ in $\Delta\phi$ and $\Delta\eta$ from $\pi^{\pm} - h^{\pm}$ correlation with $5 < p_{T,\mathrm{trig}} < 10$ GeV/c. (a) Results for d + Au. (b) Results for $p + p$. Bars are statistical errors.

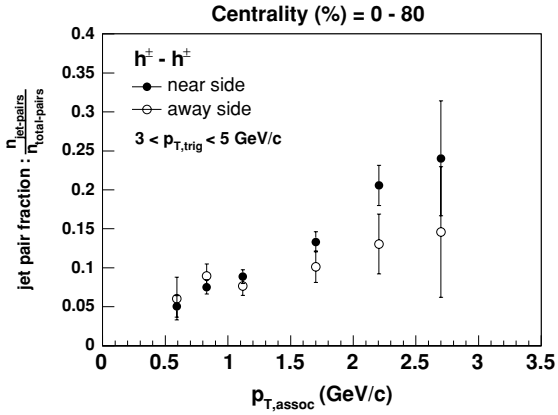

FIG. 19. Average jet pair fraction per event as a function of $p_{T,\mathrm{assoc}}$. Results are shown for the trigger hadron selection $3.0 < p_T < 5.0$ GeV/c from $d+$Au collisions and a centrality of 0−80%. Bars are statistical errors.

single-particle yields per event for trigger and associated particles, respectively. This gives the average number of jet-correlated pairs per event over the combinatoric background $n_{\mathrm{jet\,pair}}/n_{\mathrm{trig}}n_{\mathrm{assoc}}$. The conditional per-trigger yield, $n_{\mathrm{jet\,pair}}/n_{\mathrm{trig}}$, is obtained via multiplication by the efficiency corrected single-particle yield $n_{\mathrm{assoc}}^{\mathrm{eff\text{-}corr.}}$ for the selected associated p_T bin of interest;

$$\frac{n_{\mathrm{jet\,pair}}}{n_{\mathrm{trig}}} = \frac{n_{\mathrm{jet\,pair}}}{n_{\mathrm{trig}}n_{\mathrm{assoc}}} \times n_{\mathrm{assoc}}^{\mathrm{eff\text{-}corr.}}. \tag{40}$$

The per-trigger yields for hadron triggers [found using Eq. (40)] are corrected for the azimuthal acceptance and tracking efficiency but are reported within the PHENIX η acceptance for the central arms, i.e., no $R(\Delta\eta)$ correction is applied to the hadron-triggered conditional yields.

Figure 20 plots the near- and far-side invariant conditional yields extracted via Eq. (40) for different trigger p_T selections as indicated. An approximate exponential decrease with p_T is observed, i.e., there are more low-p_T particles associated with each high-p_T trigger hadron. The data are tabulated in Tables XIII and XIV.

In Fig. 21, the conditional yields for identified pion triggers are plotted as a function of $p_{T,\mathrm{assoc}}$ for both near- and far-side correlations. For this high-p_T data, the conditional yields are extracted from the fits to the data in Figs. 13 and 14 using Eq. (26), then corrected for pair efficiency in $\Delta\eta$ using Eqs. (24) and (25). The conditional yields are tabulated in Tables XV and XVI.

TABLE XIII. Near- and far-side conditional yields as a function of $p_{T,\mathrm{assoc}}$ for charged hadron triggers (2.5−4 GeV/c) and associated charged hadrons from $d+$Au collisions.

$\langle p_{T,\mathrm{assoc}}\rangle$ (GeV/c)	dN/dp_T^{near}	dN/dp_T^{far}
0.592	0.327 ± 0.092	0.383 ± 0.182
0.831	0.307 ± 0.045	0.339 ± 0.079
1.190	0.174 ± 0.018	0.158 ± 0.024
1.702	0.081 ± 0.009	0.066 ± 0.014
2.205	0.042 ± 0.006	0.028 ± 0.009

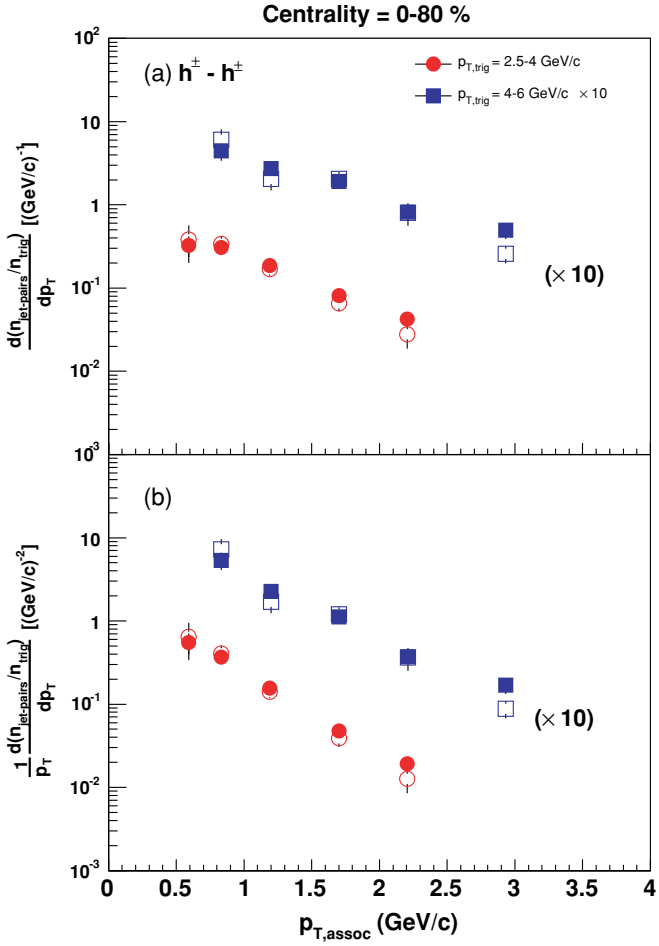

FIG. 20. (Color online) Per-trigger yield (a) and invariant conditional yield (b) as a function of $p_{T,\mathrm{assoc}}$ for the trigger hadron ranges shown. Closed points are the near-side yields; open points are the far-side yields. Centrality range is 0−80% in $d+$Au collisions. Yields are corrected for efficiency and reported in the PHENIX η acceptance. Bars are statistical errors.

The agreement between the two pion-triggered data sets is good, which indicates that the jet fragmentation function is independent of whether a neutral pion or a charged pion trigger is used. The difference in the magnitudes of the far- and near-side yields reflects the fact that the far-side correlation measure a hadron triggered effective fragmentation while the near-side correlation measures dihadron fragmentation.

The conditional yields presented in Figs. 20 and 21 can be considered as the basic information, whereas the near and far

TABLE XIV. Same as Table XIII, but for charged hadron triggers (4−6 GeV/c).

$\langle p_{T,\mathrm{assoc}}\rangle$ (GeV/c)	dN/dp_T^{near}	dN/dp_T^{far}
0.831	4.437 ± 1.040	6.031 ± 2.010
1.200	2.725 ± 0.506	2.051 ± 0.562
1.700	1.907 ± 0.278	2.046 ± 0.447
2.210	0.819 ± 0.152	0.804 ± 0.244
2.931	0.497 ± 0.107	0.258 ± 0.061

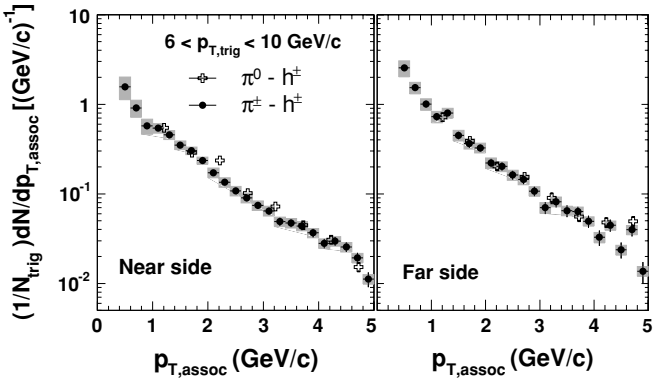

FIG. 21. Conditional yield as function of $p_{T,\mathrm{assoc}}$ for near- and far-side correlations from minimum-bias $d+$ Au collisions. Bars are statistical errors. Shaded boxes represent the total systematic error on each point.

dN/dx_E distributions in Sec. IV B have a closer relationship to parton fragmentation functions, as described in Sec. II.

Since multiple scattering should increase with centrality, we examine whether these jet characteristics exhibit any centrality dependence. Figure 22 reports on widths and conditional yields in the PHENIX η acceptance for dihadron correlations with a trigger hadron in the range $2.5 < p_{T,\mathrm{trig}} < 4$ GeV/c. The data are tabulated in Tables XVII and XVIII. Centrality-dependent widths for the $\pi^0 - h^{\pm}$ correlations are shown in Fig. 23 for a mean $\pi^0 p_T$ of approximately 5.4 GeV/c. The data for the widths are tabulated in Table XIX, while the yields can be found in Table XX.

Neither the widths nor the per-trigger yields change significantly with centrality, indicating that the influence of multiple scattering on jet properties is small in this region. This work is extended in Sec. IV D, where we present the centrality dependence of various jet-structure observables.

TABLE XV. Near- and far-side conditional yields as a function of $p_{T,\mathrm{assoc}}$ for charged pion triggers (5−10 GeV/c) and associated charged hadrons from minimum-bias $d+$ Au collisions.

$\langle p_{T,\mathrm{assoc}}\rangle$ (GeV/c)	dN/dp_T^{near}	dN/dp_T^{far}
0.5	1.57 ± 0.083	2.54 ± 0.15
0.7	0.911 ± 0.049	1.53 ± 0.13
0.9	0.574 ± 0.031	1.00 ± 0.087
1.1	0.542 ± 0.032	0.727 ± 0.068
1.3	0.456 ± 0.026	0.801 ± 0.058
1.5	0.351 ± 0.022	0.451 ± 0.044
1.7	0.303 ± 0.018	0.365 ± 0.038
1.9	0.235 ± 0.015	0.327 ± 0.031
2.1	0.172 ± 0.012	0.222 ± 0.025
2.3	0.135 ± 0.010	0.203 ± 0.022
2.5	0.108 ± 0.008	0.162 ± 0.018
2.7	0.0905 ± 0.0075	0.145 ± 0.017
2.9	0.0742 ± 0.0064	0.107 ± 0.013
3.1	0.0645 ± 0.0059	0.070 ± 0.011
3.3	0.0490 ± 0.0052	0.0819 ± 0.0113
3.5	0.0473 ± 0.0047	0.0647 ± 0.0097
3.7	0.0439 ± 0.0045	0.0636 ± 0.0084
3.9	0.0367 ± 0.0040	0.0495 ± 0.0075
4.1	0.0281 ± 0.0034	0.0327 ± 0.0064
4.3	0.0297 ± 0.0034	0.0446 ± 0.0068
4.5	0.0256 ± 0.0031	0.0238 ± 0.0048
4.7	0.0192 ± 0.0027	0.0397 ± 0.0061
4.9	0.0112 ± 0.0021	0.0137 ± 0.0036

TABLE XVI. Same as Table XV, but for neutral pion triggers.

$\langle p_{T,\mathrm{assoc}}\rangle$ (GeV/c)	dN/dp_T^{near}	dN/dp_T^{far}
1.21	0.545 ± 0.035	0.718 ± 0.076
1.71	0.289 ± 0.014	0.389 ± 0.030
2.21	0.236 ± 0.009	0.203 ± 0.018
2.72	0.102 ± 0.006	0.155 ± 0.012
3.22	0.0724 ± 0.0049	0.090 ± 0.012
3.73	0.0448 ± 0.0039	0.0560 ± 0.0071
4.23	0.0308 ± 0.0029	0.0481 ± 0.0058
4.72	0.0152 ± 0.0017	0.0495 ± 0.0060

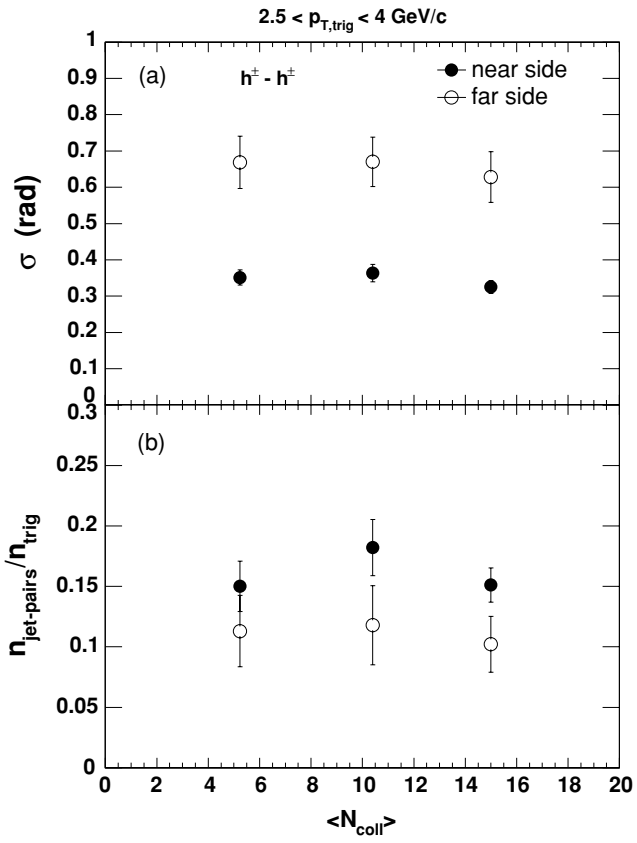

FIG. 22. Near- and far-side widths and conditional yields in the PHENIX pseudorapidity acceptance for several centrality selections from $d+$ Au collisions. Results are shown for the trigger hadron selection $2.5 < p_T < 4.0$ GeV/c and the associated p_T range of $1 < p_T < 2.5$ GeV/c. Bars are statistical errors.

TABLE XVII. Near- and far-side widths as a function of N_{coll} for charged hadron triggers (2.5−4 GeV/c) and associated charged hadrons (1–2.5 GeV/c) from d + Au collisions.

Centrality	σ_{near}(rad)	σ_{far}(rad)
0−20%	0.351 ± 0.021	0.669 ± 0.072
20−40%	0.364 ± 0.024	0.670 ± 0.068
40−80%	0.325 ± 0.018	0.628 ± 0.070

B. Jet properties in minimum-bias d + Au collisions

From the angular widths and yields discussed in the previous section, we calculate the following quantities that characterize the jet structures: transverse momentum of hadrons with respect to the jet (j_T), the dijet acoplanarity $\langle \sin^2(\phi_{jj}) \rangle$, and the dN/dx_E distributions. These quantities are first presented for minimum-bias d + Au collisions, which have the highest statistical precision, and are then compared with results from $p + p$ in Sec. IV C.

Figure 24 shows the compilation of $\sqrt{\langle j_T^2 \rangle}$ values extracted from $\pi^0 - h$ and $\pi^\pm - h$ correlations, and assorted-p_T and fixed-p_T correlation results for $h - h$ at low p_T. The $\sqrt{\langle j_T^2 \rangle}$ values were calculated using Eq. (7). The systematic errors are mainly due to the uncertainties of Eq. (7) and the fitting procedure, which are about 5% (independent of p_T) and are approximately the same for all four analyses. The $\sqrt{\langle j_T^2 \rangle}$ values for $\pi^\pm - h$ and $\pi^0 - h$ indicate a steady increase at p_T below 2 GeV/c followed by a saturation around 560−640 MeV/c at $p_T > 2$ GeV/c. The initial increase is due to the seagull effect [46,47]. The approximately constant behavior of $\sqrt{\langle j_T^2 \rangle}$ above 2 GeV/c is consistent with the scaling behavior of the fragmentation functions. The $\sqrt{\langle j_T^2 \rangle}$ results from the $h - h$ correlation analyses have a similar increase and saturation behavior. They seem to reach a slightly higher plateau value at a lower p_T (around 1.5 GeV/c).

A combined fit based on $\sqrt{\langle j_T^2 \rangle}$ data points at $p_T > 2$ GeV/c gives a plateau value of $\sqrt{\langle j_T^2 \rangle} = 0.64 \pm 0.02(\text{stat}) \pm 0.04(\text{sys})$ GeV/c for minimum-bias d + Au collisions.

TABLE XVIII. Same as Table XVII, but for near- and far-side conditional yields.

Centrality	dN/dp_T^{near}	dN/dp_T^{far}
0–20%	0.150 ± 0.021	0.113 ± 0.030
20–40%	0.182 ± 0.023	0.118 ± 0.033
40–80%	0.151 ± 0.014	0.102 ± 0.023

TABLE XIX. Near- and far-side widths as a function of centrality for neutral pion triggers (5−10 GeV/c) and associated charged hadrons (2–3 GeV/c) from d + Au collisions.

Centrality	σ_{near}(rad)	σ_{far}(rad)
0–20%	0.199 ± 0.009	0.387 ± 0.024
20–40%	0.195 ± 0.009	0.401 ± 0.031
40–88%	0.190 ± 0.008	0.376 ± 0.024

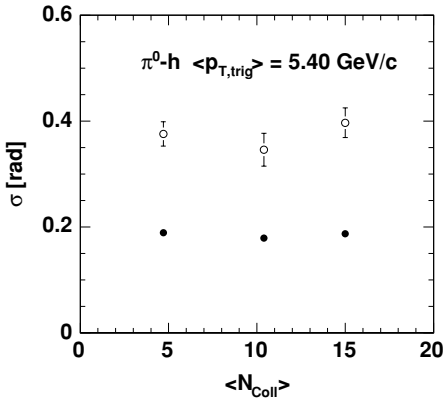

FIG. 23. Near- and far-side widths for several centrality selections from d + Au collisions. Results are shown for $\pi^0 - h$ correlations with the trigger π^0 $5 < p_T < 10$ GeV/c and the associated p_T range of $2 < p_T < 3$ GeV/c. Bars are statistical errors.

A key quantity that provides information on multiple scattering in the cold nuclear medium is $\langle \sin^2(\phi_{jj}) \rangle$, where ϕ_{jj} is the azimuthal angle between the jet axes. As described in Sec. II, we calculate $\langle \sin^2 \phi_{jj} \rangle$ from the experimental values of the near- and far-side widths [Eq. (13)]. Figure 25 shows $\langle \sin^2 \phi_{jj} \rangle$ as function of $p_{T,\text{assoc}}$ for high-p_T pion triggers. We observe that the rms of the sine of the angle between the jet axes, $\langle \sin^2 \phi_{jj} \rangle$, decreases as higher-$p_T$ associated particles are selected. There is good agreement between the two data sets. Figure 26 plots $\langle \sin^2 \phi_{jj} \rangle$ as a function of $p_{T,\text{trig}}$, where a similar decrease with p_T is observed.

In the next section we will calculate the quadrature difference $\langle \sin^2 \phi_{jj} \rangle$ between d + Au and $p + p$ collisions and use that to quantify the affect of additional final-state scattering in d + Au collisions.

In Sec. II we defined the near and far-side p_{out}. With this observable, it is possible to move beyond calculating means or rms values, and hence the p_{out} distribution potentially carries more information about the dijet acoplanarity. The measured p_{out} distributions for $\pi^\pm - h^\pm$ are shown in Fig. 27 for the near and far sides. The far-side p_{out} has a broader distribution than the near-side p_{out}, reflecting the fact that k_T is larger than j_T. The p_{out} distributions have a power law tail, possibly due to strong radiative processes driving large values of p_{out}.

In Sec. IV A we reported the yields of associated hadrons per trigger particle, or the conditional yield. A more comprehensive way of quantifying the fragmentation function is to plot the conditional yields as a function of x_E. This is shown in Fig. 28 for $\pi^\pm - h$ and $\pi^0 - h$.

TABLE XX. Same as Table XIX, but for near- and far-side conditional yields.

Centrality	dN/dp_T^{near}	dN/dp_T^{far}
0–20%	0.0816 ± 0.0037	0.116 ± 0.008
20–40%	0.0947 ± 0.0045	0.141 ± 0.011
40–88%	0.0967 ± 0.0043	0.144 ± 0.009

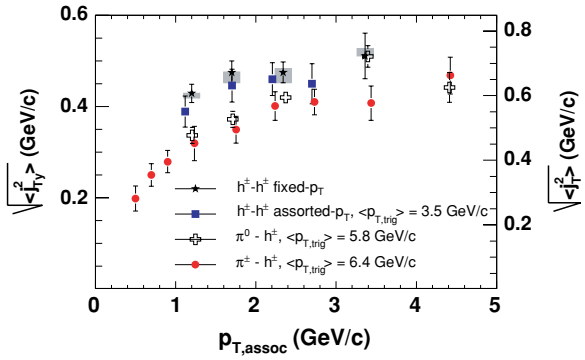

FIG. 24. (Color online) Extracted $\sqrt{\langle j_T^2 \rangle}$ for minimum-bias $d+$Au collisions from all four dihadron correlations. Trigger p_T ranges are 3–5, 5–10, and 5–10 GeV/c, respectively, for $h^\pm - h^\pm$, $\pi^0 - h^\pm$, and $\pi^\pm - h^\pm$ assorted-p_T correlations. Statistical and systematic errors are combined for the assorted-p_T correlations; the fixed-p_T correlation shows the systematic error separately as shaded boxes.

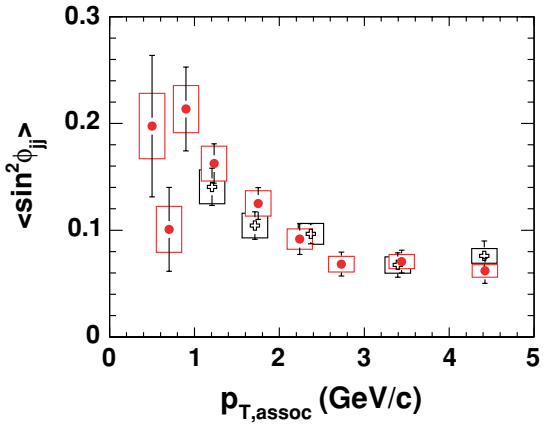

FIG. 25. (Color online) $\langle \sin^2 \phi_{jj} \rangle$ for minimum-bias $d+$Au collisions as function of associated particle p_T for $\pi^\pm - h^\pm$ (filled circles) and $\pi^0 - h^\pm$ (open crosses) correlations where the trigger particles have a p_T between 5 and 10 GeV/c. Data points are plotted at the mean $p_{T,\mathrm{assoc}}$. Bars are statistical errors. Boxes represent the total systematic error on each point.

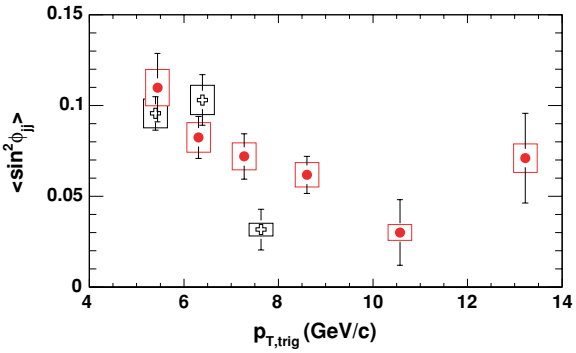

FIG. 26. (Color online) Same as Fig. 25, but as function of trigger particle p_T.

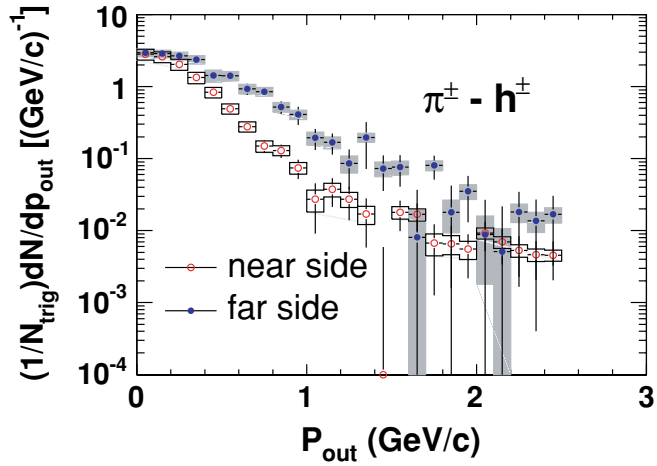

FIG. 27. (Color online) Near- and far-side p_{out} distributions for minimum-bias $d+$Au collisions obtained from $\pi^\pm - h^\pm$ correlation. The trigger is $5 < p_{T,\mathrm{trig}} < 10$ GeV/c, the associated particle is $0.5 < p_{T,\mathrm{assoc}} < 5.0$ GeV/c. Bars are statistical errors. Boxes represent the total systematic error on each point.

Previously, in ISR experiments, the slope of the x_E distribution had been determined to be around 5.3 [26]. In Fig. 29, the conditional yields as a function of x_E are plotted for the trigger p_T range of 5–6 GeV/c. In order to compare data with the previous ISR results, we determine the exponential inverse slope for $0.3 < x_E < 0.7$ and obtain the inverse slope parameter of 6.0 ± 0.3 in the near side and 7.1 ± 0.5 in the far side. The near-side x_E inverse slope is smaller than that for the far side, reflecting the difference between dihadron fragmentation and single hadron fragmentation. By requiring a trigger particle on the near side, one reduces the jet energy available for fragmenting to the second hadrons, and consequently a smaller inverse slope occurs for the near side. Note, however, that the x_E distributions do not have pure exponential shape, and the fitted inverse slope is sensitive to the fitting ranges.

It is well known that fragmentation functions $D(z)$ approximately scale in e^+e^- or $p+p$ collisions, i.e., they are

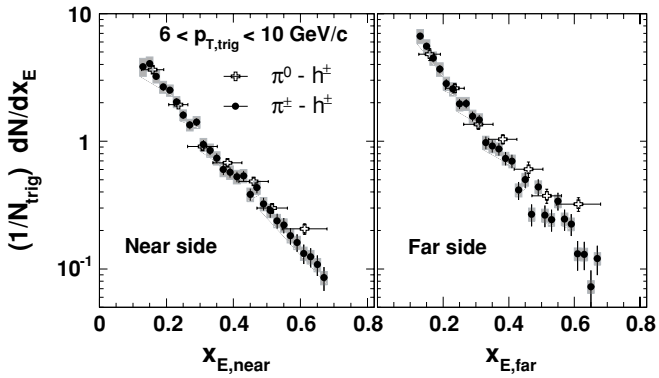

FIG. 28. Conditional yield as a function of x_E for near- and far sides for $\pi^\pm - h^\pm$ and $\pi^0 - h^\pm$ from minimum-bias $d+$Au collisions. Bars are statistical errors. Boxes represent the total systematic error on each point.

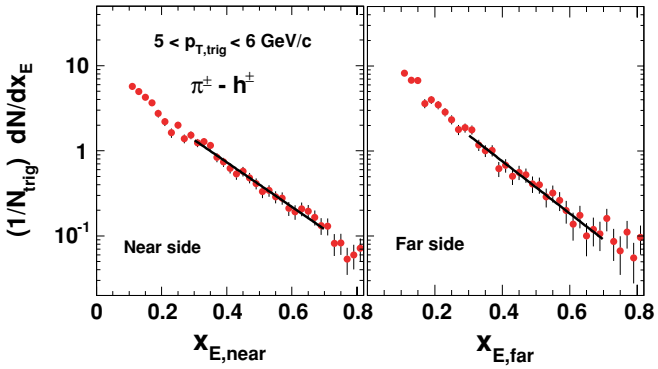

FIG. 29. (Color online) Conditional yield as a function of x_E for near- and far-side correlations for $\pi^{\pm} - h^{\pm}$ correlations from minimum-bias d + Au collisions. Trigger pions are $5 < p_{T,\mathrm{trig}} < 6$ GeV/c, and the black lines are fits to an exponential function for $0.3 < x_E < 0.7$. Bars are statistical errors.

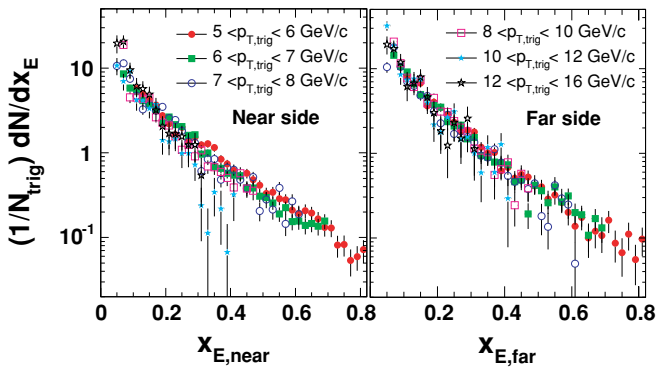

FIG. 30. (Color online) Conditional yield as a function of x_E for near- and far-side correlations for $\pi^{\pm} - h^{\pm}$ correlations for several different trigger p_T's for minimum-bias d + Au collisions. Bars are statistical errors.

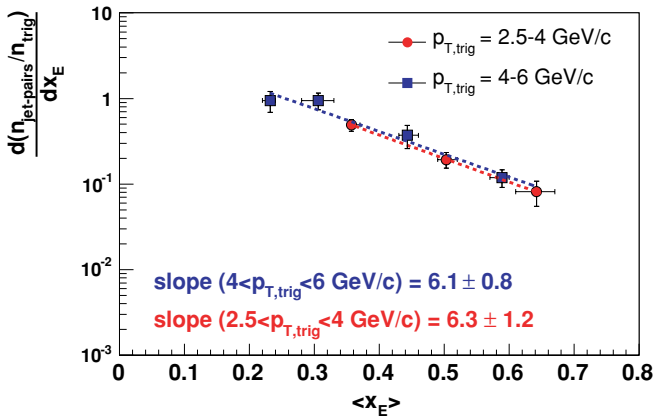

FIG. 31. (Color online) Conditional yield as a a function of $\langle x_E \rangle$ for the far-side $h - h$ correlations for two trigger p_T ranges. Dashed lines are exponential fits to the data. Bars are statistical errors.

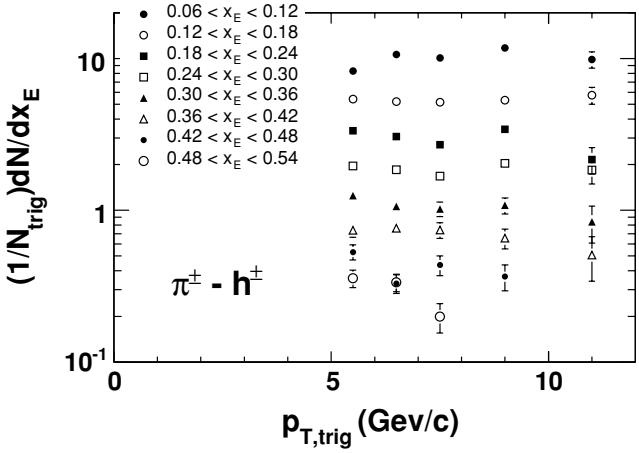

FIG. 32. Far-side conditional yield as a function of $p_{T,\mathrm{trig}}$ for different ranges of x_E for $\pi^{\pm} - h^{\pm}$ correlation for minimum-bias d + Au collisions. Bars are statistical errors.

independent of jet energy. To check whether this is still true in d + Au collisions, we plot in Fig. 30 the conditional yield as a function of x_E for different ranges of trigger p_T from $\pi^{\pm} - h^{\pm}$ correlations. All curves fall on top of each other, indicating a universal behavior of the jet fragmentation function.

At lower p_T, we have x_E distributions from the $h - h$ correlations. In Fig. 31, far-side conditional yields as obtained from charged hadron correlation functions are plotted versus $\langle x_E \rangle$. Here, $\langle x_E \rangle$ has been calculated from the $\langle p_{T,\mathrm{trig}} \rangle$, $\langle p_{T,\mathrm{assoc}} \rangle$ and extracted angular widths. Results are shown for two trigger p_T ranges, $2.5 < p_{T,\mathrm{trig}} < 4$ GeV/c and $4 < p_{T,\mathrm{trig}} < 6$ GeV/c, respectively. The slopes extracted are 6.3 ± 1.2 for the lower trigger p_T range and 6.1 ± 0.8 for the higher trigger p_T window. Within the statistics of the charged hadron data set, we do not observe a strong sensitivity of the slope of the x_E distributions to the trigger p_T.

A direct way of quantifying the scale dependence of the x_E distribution is to plot the far-side conditional yields versus $p_{T,\mathrm{trig}}$ for a fixed range of x_E. This is shown in Fig. 32, where the conditional yields are found to be independent of $p_{T,\mathrm{trig}}$, i.e., there is no significant deviation from scaling. We will quantify any scaling violation in these data when we compare these x_E distributions from d + Au to distributions from $p + p$ collisions in Sec. IV C.

C. Comparison between d + Au and $p + p$

As discussed in Sec. I, multiple scattering in the cold nuclear medium may broaden the far-side correlation and possibly modify the fragmentation properties. In the previous section, we presented the measured jet structures from minimum-bias d + Au collisions. In this section, we compare that data to results from $p + p$ collisions. The goal is to establish the extent to which the nuclear medium modifies the properties of jets.

Figure 33 compares the extracted $\sqrt{\langle j_T^2 \rangle}$ values as functions of $p_{T,\mathrm{assoc}}$ from d + Au and $p + p$ collisions. The $\sqrt{\langle j_T^2 \rangle}$ values show no change from $p + p$ to d + Au collisions.

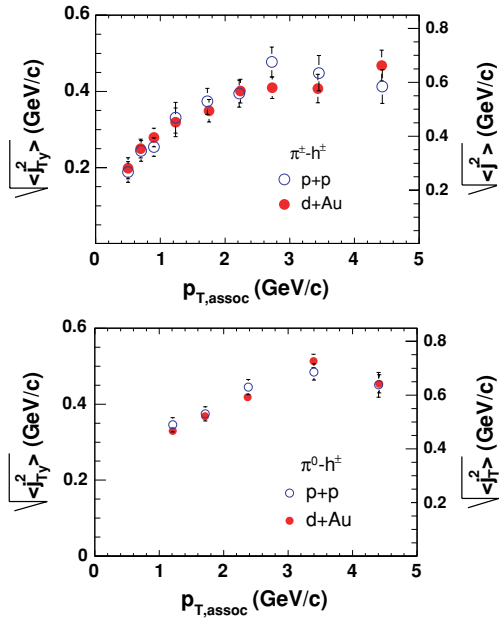

FIG. 33. (Color online) Comparison of $\sqrt{\langle j_T^2 \rangle}$ values between $d+$ Au and $p+p$ for $\pi^{\pm}-h^{\pm}$ and $\pi^0-h^{\pm}$ correlations. Trigger pion range is 5–10 GeV/c. Bars are statistical errors. Systematic errors are given in Table III.

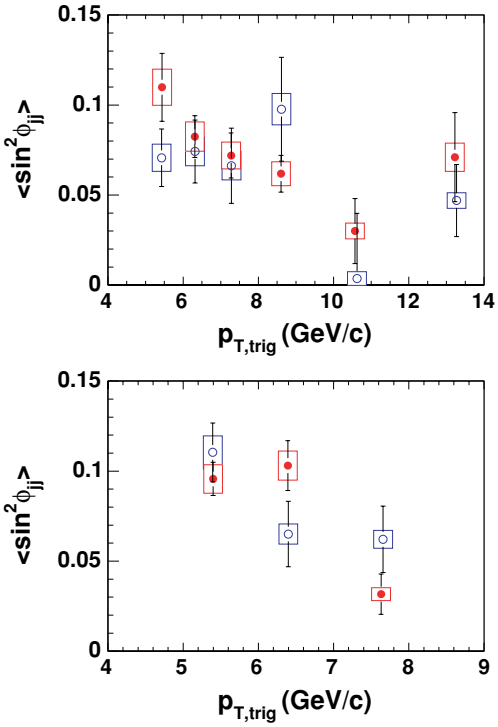

FIG. 34. (Color online) Comparison of $\langle \sin^2(\phi_{jj}) \rangle$ values between $d+$ Au (filled circles) and $p+p$ (open circles) for $\pi^{\pm}-h^{\pm}$ correlations (top panel) and $\pi^0-h^{\pm}$ correlations (lower panel). Associated hadron range is $2 < p_{T,\mathrm{assoc}} < 4.5$ GeV/c for the charged pion triggers and $2.5 < p_{T,\mathrm{assoc}} < 5$ GeV/c for the neutral pions. Bars are statistical errors. Boxes represent the total systematic error on each point.

Similarly, the $\langle \sin^2(\phi_{jj}) \rangle$ values shown in Fig. 34 for $d+$ Au are comparable to those from $p+p$ within errors, although the values from $d+$ Au collisions are systematically higher for $\pi^{\pm}-h^{\pm}$. Since there is no strong difference between the $d+$Au and $p+p$ results, there is little indication for increased multiple scattering in the $d+$ Au final state.

Any additional radiation can be quantified by calculating the point-by-point quadrature difference in $\langle \sin^2 \phi_{jj} \rangle$ between $d+$ Au and $p+p$ collisions. As shown in Fig. 35, this difference is consistent with zero. The average value for π^0-h is $\Delta\langle \sin^2 \phi_{jj} \rangle = -0.005 \pm 0.012(\mathrm{stat}) \pm 0.003(\mathrm{sys})$; for $\pi^{\pm}-h$, $\Delta\langle \sin^2 \phi_{jj} \rangle = 0.011 \pm 0.011(\mathrm{stat}) \pm 0.010(\mathrm{sys})$. Combining the two data sets, we find $\Delta\langle \sin^2 \phi_{jj} \rangle = +0.004 \pm 0.008(\mathrm{stat}) \pm 0.009(\mathrm{sys})$.

Figure 36 shows the comparison of the p_{out} distribution between central $d+$Au and $p+p$ from $\pi^{\pm}-h^{\pm}$ correlations; no apparent differences are observed in either the near or far side. This is consistent with the observation that both $\sqrt{\langle j_T^2 \rangle}$ and $\langle \sin^2 \phi_{jj} \rangle$ are similar between $d+$ Au and $p+p$.

A second set of comparisons between $d+$ Au and $p+p$ collisions is the number of hadrons in the near- and far-angle jet structures associated with a high-p_T trigger. Figure 37 shows the comparison of the conditional yield as function of x_E and no apparent difference between $d+$ Au and $p+p$ collisions is observed for either the near or far side.

In the previous section, we examined the level of scaling violations in the far-side dN/dx_E distribution for $d+$ Au collisions by plotting different x_E ranges as a function of $p_{T,\mathrm{trig}}$ (Fig. 32). The comparable plot for $p+p$ collisions is shown in Fig. 38. For both $d+$ Au and $p+p$ collisions, the amount of scaling violations, i.e., the dependence of dN/dx_E on $p_{T,\mathrm{trig}}$, can be quantified by fitting the data in each x_E range with a straight line as a function of $p_{T,\mathrm{trig}}$, that is,

$$\frac{dN}{dx_E} = \frac{dN}{dx_{E\,0}}(1+\beta p_T). \tag{41}$$

The fitted slopes β represent the fractional change in dN/dx_E per GeV/c and are shown in Fig. 39. For the $d+$ Au data,

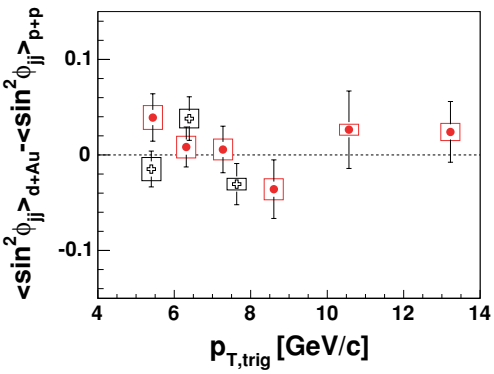

FIG. 35. (Color online) Quadrature difference between minimum-bias $d+$ Au and $p+p$ $\langle \sin^2 \phi_{jj} \rangle$ values. Closed circles are $\pi^{\pm}-h$ values and the open circles are π^0-h values. Bars are statistical errors. Boxes represent the total systematic error on each point.

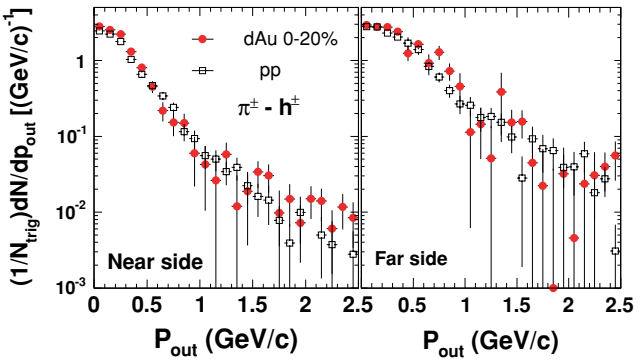

FIG. 36. (Color online) Comparison of the $p_{\rm out}$ distribution at the near and far sides between central $d+{\rm Au}$ collisions and $p+p$ collisions. Results are obtained for $\pi^{\pm}-h^{\pm}$ correlations with the associated hadron range $0.5 < p_{T,\rm assoc} < 5$ GeV/c and trigger pion range of $5 < p_{T,\rm trig} < 10$ GeV/c. Bars are statistical errors.

β is consistent with zero, i.e., there is no significant scaling violation across the whole x_E range, while there may be a slight scaling violation at high x_E for the $p+p$ data. On a point-by-point basis, there is no systematic difference between the $d+{\rm Au}$ and $p+p$ data.

Taken as a whole, all the results presented in this section indicate that the presence of the cold nuclear medium causes no significant change in jet fragmentation between $d+{\rm Au}$ and $p+p$ collisions. In addition, no strong evidence supports an increase in $\langle\sin^2(\phi_{jj})\rangle$ due to multiple scattering in the Au nucleus. Using the minimum-bias $d+{\rm Au}$ data has the advantage of the highest statistical precision. In the next section, we examine whether there is any change in jet structures as a function of collision centrality in $d+{\rm Au}$, i.e., we split the statistics into a few centrality classes to increase the lever arm of the nuclear thickness function.

D. Centrality dependence

As discussed in Sec. I, $\langle\sin^2(\phi_{jj})\rangle$ is expected to increase as $d+{\rm Au}$ collisions become more central because of increased multiple scattering. Models of multiple scattering [12] predict that the increase in $\langle k_T^2\rangle$ is proportional to $T_A(b)$, the nuclear

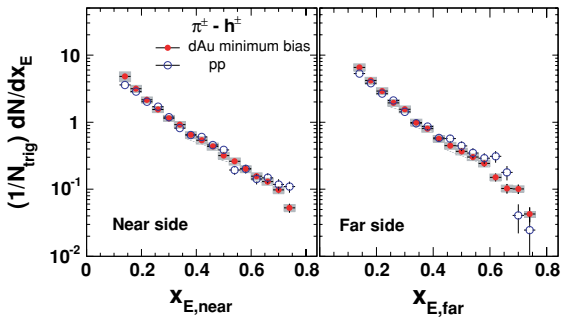

FIG. 37. (Color online) Comparison of the x_E distribution from $\pi^{\pm}-h^{\pm}$ correlations at the near and far sides between minimum-bias $d+{\rm Au}$ collisions and $p+p$ collisions. Triggers are $\pi^{\pm}$ from 5−10 GeV/c. Bars are statistical errors. Boxes represent the total systematic error on each point.

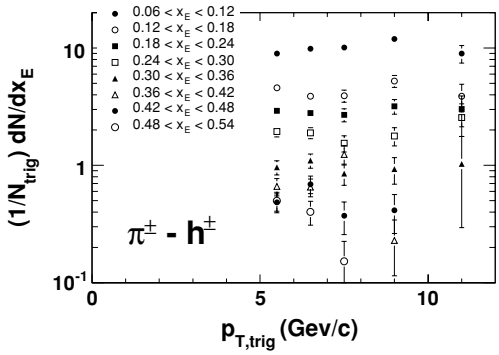

FIG. 38. Far-side conditional yield as function of $p_{T,\rm trig}$ for different ranges of x_E from $p+p$ collisions; triggers are $\pi^{\pm}$ from 5−10 GeV/c. Bars are statistical errors.

thickness function. We are not aware of predictions of how $\langle\sin^2(\phi_{jj})\rangle$ will change with centrality, but note that any increase in $\langle k_T^2\rangle$ will also increase $\langle\sin^2(\phi_{jj})\rangle$.

To probe this physics, we measured angular correlations in three centrality bins for $d+{\rm Au}$ collisions (0–20%, 20–40%, and 40–88%) to extract angular widths of the jet structures and hence $\sqrt{\langle j_T^2\rangle}$ and $\langle\sin^2(\phi_{jj})\rangle$. Figure 40 shows the independent data sets of $\langle\sin^2(\phi_{jj})\rangle$ including results from $p+p$ collisions and the three centrality classes from $d+{\rm Au}$ collisions.

All the $\langle\sin^2(\phi_{jj})\rangle$ data in Fig. 40 have been simultaneously fit with the following linear equation in $T_A(b)$:

$$\langle\sin^2(\phi_{jj})\rangle = \langle\sin^2(\phi_{jj})\rangle_0(1+a_{\rm frac}T_A(b)). \qquad (42)$$

The slope parameter $a_{\rm frac}$ is assumed to be common to all data sets, while the pre-factors $\langle\sin^2(\phi_{jj})\rangle_0$ depend on the p_T of the trigger and associated particles. The extracted slope $a_{\rm frac} = -0.01 \pm 0.40$ mb with χ-squared per degree of freedom, $\chi^2/\nu = 27/22$. This slope is consistent with zero; i.e., we do not observe any significant increase in $\langle\sin^2(\phi_{jj})\rangle$ with centrality.

This can be compared to predictions from Hwa and Yang [16], who assume no increase in k_T with centrality to reproduce the Cronin effect data at RHIC, and Qiu and Vitev [14], who calculate

$$\langle k_T^2\rangle_{\rm dijet} = 2\langle k_T^2\rangle_{\rm vac} + \frac{0.72}{T_{A\,\rm minbias}}T_A(b). \qquad (43)$$

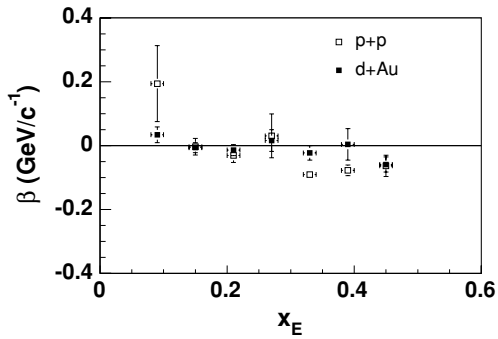

FIG. 39. Fitted fractional change in dN/dx_E per unit $p_{T,\rm trig}$ [β in Eq. (41)] of the far-side conditional yield for different ranges of x_E. Bars are statistical errors.

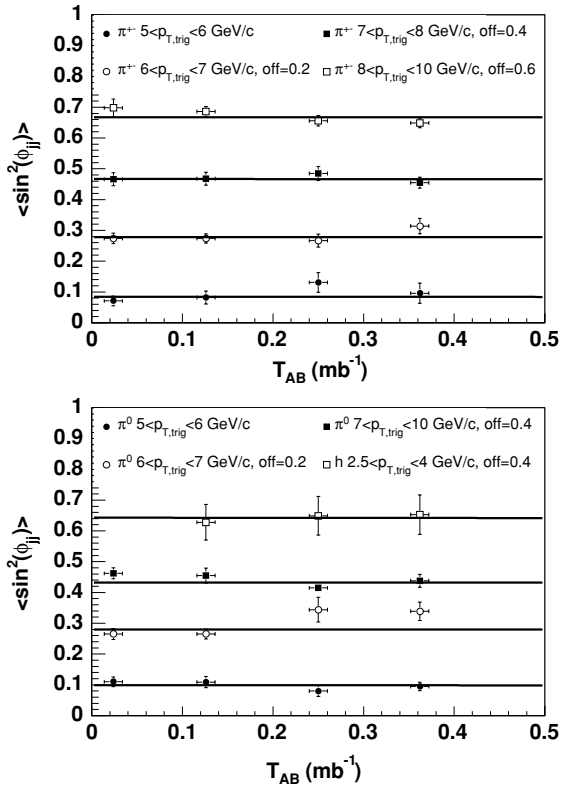

FIG. 40. Measured values of $\langle \sin^2(\phi_{jj})\rangle$ as a function of the nuclear thickness function $T_A(b)$. Left-most points are from $p+p$ collisions; other points are from the three centrality classes in $d+$Au collisions. Data sets are offset as indicated for clarity. Top plot shows data for $\pi^{\pm}$; bottom plot, for π^0 and hadron triggered data. Lines are a simultaneous fit to all the data with Eq. (42) to extract a common fractional increase in $\langle \sin^2(\phi_{jj})\rangle$ with $T_A(b)$. Bars are statistical errors.

To gain some insight into the magnitude of Qiu and Vitev's predicted effect compared to our experimental results, we recast Eq. (43) into the same form as Eq. (42).

$$\langle k_T^2\rangle_{\rm dijet} = 2\langle k_T^2\rangle_{\rm vac}\left(1+\frac{0.72}{2\langle k_T^2\rangle_{\rm vac} T_{A\,\rm minbias}}T_A(b)\right). \quad (44)$$

Hence, their prediction for the fractional increase in $\langle k_T^2\rangle$ with $T_A(b)$ is from 0.51 to 0.72 depending on the range $0.25 < \langle k_T^2\rangle_{\rm vac} < 0.35$ (GeV/c)^2 suggested by Qiu and Vitev [14].[4] Though the predicted fractional increase is of a different quantity, it should provide an estimate of the magnitude of the fractional increase in $\langle \sin^2(\phi_{jj})\rangle$. The prediction is slightly larger than one standard deviation (statistical) from our experimental result, $a_{\rm frac} = -0.01 \pm 0.40$ mb. If the measured value for $\langle k_T^2\rangle_{\rm vac}$ at RHIC turns out to be larger than assumed by Qiu and Vitev [14], then the predicted fractional increase in Eq. (44) will be smaller.

Barnafoldi *et al.* [15] have also predicted the increase in k_T due to multiple scattering in $d+$Au collisions at RHIC. They calculated that $\langle k_T^2\rangle$ increases by $C = 0.35$(GeV/c)^2 per collision up to the first four collisions, then it saturates. Their prediction is

$$\langle k_T^2\rangle = \langle k_T^2\rangle_0\left(1+\frac{0.35}{\langle k_T^2\rangle_0}(40\times T_A)\right), \qquad T_A < 0.1,$$
$$\langle k_T^2\rangle = \langle k_T^2\rangle_0\left(1+\frac{0.35}{\langle k_T^2\rangle_0}(40\times 0.1)\right), \qquad T_A > 0.1. \quad (45)$$

Barnafoldi *et al.* do not provide values for $\langle k_T^2\rangle_0$; however, if we use the range $0.25 < \langle k_T^2\rangle_0 < 0.35$ (GeV/c)^2 suggested by Qiu and Vitev [14] then the fractional increase with T_A is 40 to 56 for $T_A < 0.1$ followed by no further increase. This rapid increase is not observable in our data set because the model saturates already in the most peripheral $d+$Au bin, where $\langle T_A\rangle = 0.11$ mb^{-1}.

As discussed in Sec. I, inelastic scattering of the hard parton in the cold medium may also increase the conditional yields (CY) of hadrons that are associated with a high-p_T trigger. Figure 41 shows the centrality dependence of the extracted CY, together with CY from $p+p$ collisions. The difference can be better illustrated by taking the ratio ($d+$Au/$p+p$) of the per-trigger yield as shown in Fig. 42. There is a possible increase in near-side particle yield for $p_T < 1$ GeV/c in the $d+$Au collisions. In other momentum ranges, there is no consistent difference between yields in $d+$Au and $p+p$ collisions. The recombination model of Ref. [22] predicted a factor of 2 increase in CY peripheral to central $d+$Au collisions which is much larger than observed in the data. A later recombination calculation by the same authors [23] using

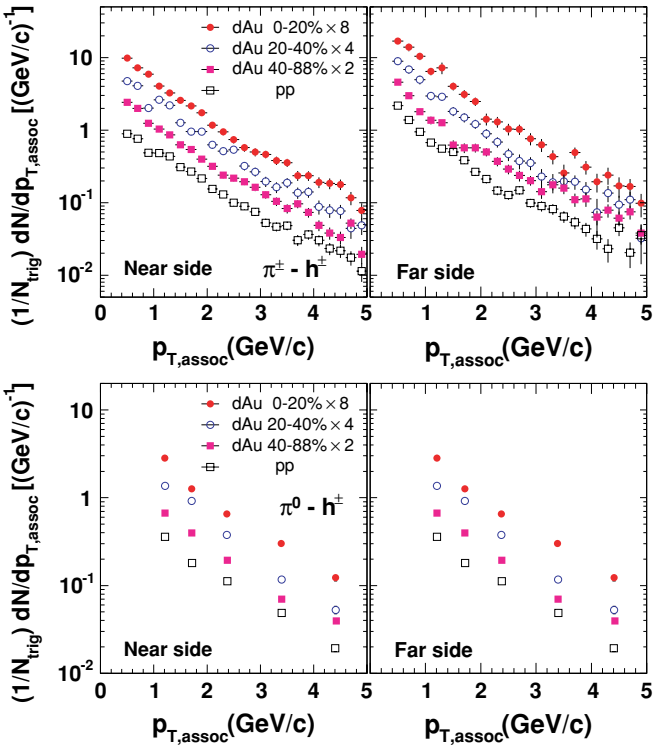

FIG. 41. (Color online) Centrality dependence of near and far CY(p_T) for $\pi^{\pm}-h^{\pm}$ and $\pi^0-h^{\pm}$ correlations. Bars are statistical errors.

[4]For 0−88% $d+$Au collisions, $T_{A\,\rm minbias} = 0.20$ mb^{-1}.

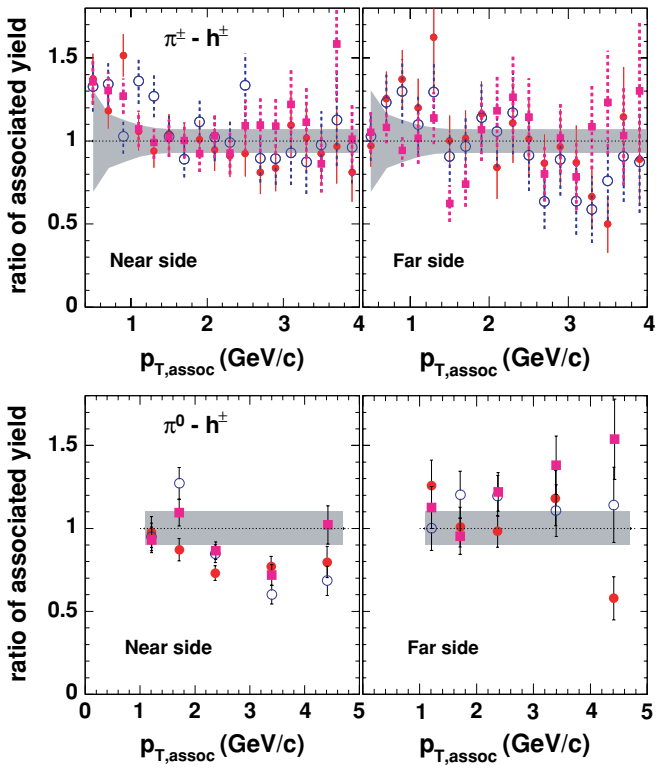

FIG. 42. (Color online) Centrality dependence related to the ratio of near and far CY(p_T) for d + Au to $p + p$ from the $\pi^{\pm} - h^{\pm}$ and $\pi^0 - h^{\pm}$ correlations. Shaded bands are the systematic errors due to normalization of the yields. Symbols are the same as in Fig. 41.

the same definition as the experiment [Eq. (16)] postdicted only a 30% increase in CY for associated particles at $p_T = 2$ GeV/c, which is comparable to or perhaps slightly larger than observed in the data.

V. CONCLUSIONS

We have measured several properties of jet fragmentation and dijet correlations using two-particle correlations with three different particle combinations: $h^{\pm} - h^{\pm}$, $\pi^0 - h^{\pm}$, and $\pi^{\pm} - h^{\pm}$. From the correlation functions, we have extracted the widths of the near- and far-angle correlations as a function of the momentum of the two hadrons, $p_{T,\mathrm{trig}}$ and $p_{T,\mathrm{assoc}}$. These widths decrease as a function of both the trigger and associated particle's momenta. From the near-angle widths, we calculate $\sqrt{\langle j_T^2 \rangle}$, the rms of the transverse momentum of fragmented hadrons with respect to the hard parton. The value of $\sqrt{\langle j_T^2 \rangle}$ saturates at $0.64 \pm 0.02(\mathrm{stat}) \pm 0.04(\mathrm{sys})$ GeV/c for $p_{T,\mathrm{assoc}} > 2$ GeV/c and is consistent with being independent of $p_{T,\mathrm{trig}}$ and trigger species. The $\sqrt{\langle j_T^2 \rangle}$ is similar for d + Au and $p + p$ collisions, which is consistent with the fragmentation process not being affected by the presence of the cold nuclear medium.

We have also compared the measured x_E distributions in d + Au collisions to the baseline distributions from $p + p$ collisions. The x_E distributions extracted from the far-angle correlations provide information on the fragmentation of a back-to-back parton triggered on a high-p_T hadron in the opposite hemisphere. The measured dN_{far}/dx_E distributions in d + Au are approximately independent of $p_{T,\mathrm{trig}}$; i.e., they scale. We have quantified the level of scaling violation by extracting the slope $\beta = d(dN/dx_E)/dp_{T,\mathrm{trig}}$ for different ranges of x_E. The slopes are consistent with zero for d + Au collisions; i.e., there is no significant scaling violation. Point by point, the scaling-violation slopes for $p + p$ collisions are not significantly different than the d + Au data. This suggests that if there is any additional gluon radiation in d + Au reactions due to multiple scattering, then it has little observable influence on the fragmentation of the hard parton.

We observe no centrality dependence of the conditional yield in d + Au, and these yields are very similar to those from $p + p$ collisions. The recombination model of Ref. [23] postdicted a 30% increase in conditional yield between d + Au and $p + p$, which is perhaps slightly larger than observed in the data.

We have extracted the dijet acoplanarity $\langle \sin^2(\phi_{jj}) \rangle$ from the widths of the back-to-back correlations in d + Au and $p + p$ collisions. In collisions involving nuclei, multiple interactions within the nucleus would tend to increase the parton transverse momentum which would be observable as a larger dijet acoplanarity; i.e., the back-to-back distribution of jets should broaden. However, in d + Au collisions, the extracted values of $\langle \sin^2(\phi_{jj}) \rangle$ are very similar to those observed in $p + p$ collisions. Indeed, the quadrature difference Δ between $\langle \sin^2(\phi_{jj}) \rangle$ in d + Au and $p + p$ is consistent with zero, $\Delta \langle \sin^2(\phi_{jj}) \rangle = +0.004 \pm 0.008(\mathrm{stat}) \pm 0.000(\mathrm{sys})$. The extracted $\langle \sin^2(\phi_{jj}) \rangle$ is also measured to be independent of the nuclear thickness function $T_A(b)$, which is in contrast to the strong A dependence of k_T observed at lower beam energies [7–9].

We have compared the centrality dependence of the extracted $\langle \sin^2(\phi_{jj}) \rangle$ with the multiple-scattering model of Qiu and Vitev [14]. This model reproduces the measured Cronin effect of single-particle spectra at RHIC [2–4] and predicts a finite increase of k_T with nuclear thickness function. When converted to a fractional increase, the prediction is at a level that is within the experimental uncertainty of the current data. Hence, our present data on $\langle \sin^2(\phi_{jj}) \rangle$ are not inconsistent with the level of multiple scattering deduced from the single-particle Cronin effect.

Taken together, we observe no change in fragmentation and no indication of the effects of multiple scattering; i.e., the jet structures are very similar in d + Au and $p + p$ collisions at RHIC energies. Our measurements also provide a critical baseline for jet measurements in Au + Au collisions at RHIC.

ACKNOWLEDGMENTS

We thank the staff of the Collider-Accelerator and Physics Departments at Brookhaven National Laboratory and the staff of the other PHENIX participating institutions for their vital contributions. We acknowledge support from the Department of Energy, Office of Science, Nuclear Physics Division, the National Science Foundation, Abilene Christian University Research Council, Research Foundation of SUNY, and Dean of the College of Arts and Sciences, Vanderbilt University

(U.S.A); Ministry of Education, Culture, Sports, Science, and Technology and the Japan Society for the Promotion of Science (Japan); Conselho Nacional de Desenvolvimento Científico e Tecnológico and Fundação de Amparo à Pesquisa do Estado de São Paulo (Brazil); Natural Science Foundation of China (People's Republic of China); Centre National de la Recherche Scientifique, Commissariat à l'Énergie Atomique, Institut National de Physique Nucléaire et de Physique des Particules, and Association pour la Recherche et le Développement des Méthodes et Processus Industriels (France); Ministry of Industry, Science and Tekhnologies, Bundesministerium für Bildung und Forschung, Deutscher Akademischer Austausch Dienst, and Alexander von Humboldt Stiftung (Germany); Hungarian National Science Fund, OTKA (Hungary); Department of Atomic Energy and Department of Science and Technology (India); Israel Science Foundation (Israel); Korea Research Foundation and Center for High Energy Physics (Korea); Russian Ministry of Industry, Science and Tekhnologies, Russian Academy of Science, Russian Ministry of Atomic Energy (Russia); VR and the Wallenberg Foundation (Sweden); the U.S. Civilian Research and Development Foundation for the Independent States of the Former Soviet Union; the US-Hungarian NSF-OTKA-MTA; and the US-Israel Binational Science Foundation.

[1] J. W. Cronin *et al*., Phys. Rev. D **11**, 3105 (1975).
[2] S. S. Adler *et al*. (PHENIX Collaboration), Phys. Rev. Lett. **91**, 072303 (2003).
[3] J. Adams *et al*. (STAR Collaboration), Phys. Rev. Lett. **91**, 072304 (2003).
[4] B. B. Back *et al*. (PHOBOS Collaboration), Phys. Rev. Lett. **91**, 072302 (2003).
[5] M. Della Negra *et al*. (CERN-College de France-Heidelberg-Karlsruhe Collaboration), Nucl. Phys. **B127**, 1 (1977).
[6] R. P. Feynman, R. D. Field, and G. C. Fox, Phys. Rev. D **18**, 3320 (1978).
[7] C. Stewart *et al*. (Fermilab E557 Collaboration), Phys. Rev. D **42**, 1385 (1990).
[8] M. D. Corcoran *et al*. (Fermilab E609 Collaboration), Phys. Lett. **B259**, 209 (1991).
[9] D. Naples *et al*., Phys. Rev. Lett. **72**, 2341 (1994).
[10] A. Angelis *et al*., Phys. Lett. **B97**, 163 (1980).
[11] M. R. Adams *et al*., Phys. Rev. Lett. **72**, 466 (1994).
[12] A. Accardi (2002), hep-ph/0212148.
[13] X. N. Wang, Phys. Rev. C **61**, 064910 (2000).
[14] J.-W. Qiu and I. Vitev, Phys. Lett. **B632**, 507 (2006).
[15] G. G. Barnafoldi, G. Papp, P. Levai, and G. Fai, J. Phys. G **30**, S1125 (2004).
[16] R. C. Hwa and C. B. Yang, Phys. Rev. Lett. **93**, 082302 (2004).
[17] R. J. Fisk *et al*., Phys. Rev. Lett. **40**, 984 (1978).
[18] M. Jacob, rapporteur's talk given at EPS Int. Conf, Geneva, Switzerland, Jun 27–Jul 4, 1979.
[19] A. L. S. Angelis *et al*. (CERN-Columbia-Oxford-Rockefeller Collaboration), Phys. Scripta **19**, 116 (1979).
[20] G. Abbiendi *et al*. (OPAL Collaboration), Eur. Phys. J. C **37**, 25 (2004).
[21] B. A. Kniehl, G. Kramer, and B. Potter, Nucl. Phys. **B582**, 514 (2000).
[22] R. C. Hwa and C. B. Yang, Phys. Rev. C **70**, 054902 (2004).
[23] R. C. Hwa and Z. Tan, Phys. Rev. C **72**, 057902 (2005).
[24] J. Huth *et al*., in *Proceedings of Research Directions for the Decade: Snowmass 1990*, edited by E. Berger (World Scientific, Singapore, 1992), p. 134.
[25] S. Catani, Y. L. Dokshitzer, M. H. Seymour, and B. R. Webber, Nucl. Phys. **B406**, 187 (1993).
[26] A. Angelis *et al*., Nucl. Phys. **B209**, 284 (1982).
[27] C. Adler *et al*. (STAR Collaboration), Phys. Rev. Lett. **90**, 032301 (2003).
[28] C. Adler *et al*. (STAR Collaboration), Phys. Rev. Lett. **90**, 082302 (2003).
[29] J. Rak, J. Phys. G **30**, S1309 (2004).
[30] S. S. Adler *et al*. (PHENIX Collaboration), Phys. Rev. C **71**, 051902 (2005).
[31] N. N. Ajitanand (PHENIX Collaboration), Nucl. Phys. **A715**, 765 (2003).
[32] J. Jia, J. Phys. G **31**, S521 (2005).
[33] P. Constantin, Ph.D. thesis, Iowa State University, 2004.
[34] K. Adcox *et al*. (PHENIX Collaboration), Nucl. Instrum. Methods A **499**, 469 (2003).
[35] M. Allen *et al*. (PHENIX Collaboration), Nucl. Instrum. Methods A **499**, 549 (2003).
[36] L. Aphecetche *et al*. (PHENIX Collaboration), Nucl. Instrum. Methods A **499**, 521 (2003).
[37] K. Adcox *et al*. (PHENIX Collaboration), Nucl. Instrum. Methods A **499**, 489 (2003).
[38] J. T. Mitchell *et al*. (PHENIX Collaboration), Nucl. Instrum. Methods A **482**, 491 (2002).
[39] S. S. Adler *et al*. (PHENIX Collaboration), Phys. Rev. C **69**, 034910 (2004).
[40] M. Aizawa *et al*. (PHENIX Collaboration), Nucl. Instrum. Methods A **499**, 508 (2003).
[41] S. S. Adler *et al*. (PHENIX Collaboration), Phys. Rev. Lett. **94**, 082301 (2005).
[42] T. Sjöstrand, L. Lönnblad, and S. Mrenna (2001), hep-ph/0108264.
[43] J. Adams *et al*. (STAR Collaboration), Phys. Rev. C **70**, 064907 (2004).
[44] P. Stankus, PHENIX Technical Note 412 (to be published).
[45] N. N. Ajitanand, J. Alexander, P. Chung, W. Holzmann, M. Issah, R. Lacey, A. Shevel, and Ataranenkopd Anielewicz, Phys. Rev. C **72**, 011902(R) (2005).
[46] G. van Apeldoorn, R. Blokzijl, D. Holthuizen, B. Jongejans, J. Kluyver, J. Warmerdam-de Leeuw, W. Metzger, H. Tiecke, and J. Timmermans, Nucl. Phys. **B91**, 1 (1975).
[47] N. M. Agababyan *et al*. (EHS-NA22 Collaboration), Phys. Lett. **B320**, 411 (1994).